

SN 2019tua : A Type IIb Supernova with Multiple Bumps in the Light Curves

XIN-BO HUANG,^{1,2} XIANG-GAO WANG,^{1,2} LONG LI,³ LI-PING XIN,⁴ JING WANG,^{1,4} TIAN-CI ZHENG,^{1,2} QI WANG,^{1,2}
HUI-YA LIU,^{1,2} ZI-MIN ZHOU,^{1,2} XIAO-MENG LU,⁴ JIAN-YAN WEI,⁴ AND EN-WEI LIANG^{1,2}

¹*Guangxi Key Laboratory for Relativistic Astrophysics, School of Physical Science and Technology, Guangxi University, Nanning, 530004, People's Republic of China*

²*GXU-NAOC Center for Astrophysics and Space Sciences, Nanning, 530004, People's Republic of China*

³*Department of Astronomy, University of Science and Technology of China, Hefei, 230026, People's Republic of China*

⁴*CAS Key Laboratory of Space Astronomy and Technology, National Astronomical Observatories, Chinese Academy of Sciences, Beijing, 100101, People's Republic of China*

ABSTRACT

We present photometric and spectroscopic observations and analysis of the type IIb supernova (SN) SN 2019tua, which exhibits multiple bumps in its declining light curves between 40 and 65 days after discovery. SN 2019tua shows a time to peak of about 25 days similar to other type IIb SNe. Our observations indicate a decrease in its brightness of about 1 magnitude in the 60 days after the peak. At about days 50, and 60, its multiband light curves exhibit bumpy behavior. The complex luminosity evolution of SN 2019tua could not be well modeled with a single currently popular energy source model, e.g., radioactive decay of ⁵⁶Ni, magnetar, interaction between the ejecta and a circumstellar shell. Even though the magnetar model has a smaller χ^2/dof value, the complex changes in SN 2019tua's brightness suggest that more than one physical process might be involved. We propose a hybrid CSM interaction plus ⁵⁶Ni model to explain the bolometric light curve (LC) of SN 2019tua. The fitting results show that the ejecta mass $M_{\text{ej}} \approx 2.4 M_{\odot}$, the total CSM mass $M_{\text{CSM}} \approx 1.0 M_{\odot}$, and the ⁵⁶Ni mass $M_{\text{Ni}} \approx 0.4 M_{\odot}$. The total kinetic energy of the ejecta is $E_k \approx 0.5 \times 10^{51}$ erg. Pre-existing multiple shells suggest that the progenitor of SN 2019tua experienced mass ejections within approximately $\sim 6 - 44$ years prior to the explosion.

Keywords: Supernovae: individual (SN 2019tua); Circumstellar matter

1. INTRODUCTION

Supernovae (SNe), among the most luminous events in stellar evolution, are classified into distinct types based on their spectral characteristics and underlying explosion mechanisms. A notable subclass is type IIb SNe, which initially exhibit hydrogen lines in their spectra, later transitioning to helium-dominated features. This spectral evolution reflects the unique nature of their progenitors, stars that have retained just enough hydrogen to display its spectral lines post-explosion, but with hydrogen envelopes so depleted that helium lines eventually prevail. Type IIb SNe, thus, occupy a critical position in the study of massive star evolution and SN physics, offering insights into the processes driving

the loss of stellar outer layers (see e.g., Filippenko 1997; Podsiadlowski et al. 1993).

The light curves (LCs) of type IIb SNe are governed by the complex interplay of nuclear decay and dynamical processes. The predominant energy source in the later stages is the radioactive decay of ⁵⁶Ni to ⁵⁶Co, and ultimately to ⁵⁶Fe (e.g., Woosley et al. 1994; Nomoto et al. 1995). Some type IIb SNe exhibit double-peaked LCs, characterized by a rapidly rising and falling peak before the main peak driven by ⁵⁶Ni. The early emission is attributed to shock-cooling emission from the heated extended envelope of the progenitor, and is observed in some cases such as SN 1993J (Richmond et al. 1994; Woosley et al. 1994), SN 2011dh (Arcavi et al. 2011; Soderberg et al. 2012; Ergon et al. 2014), SN 2013df (Morales-Garoffolo et al. 2014; Van Dyk et al. 2014), SN 2016gkg (Nayana et al. 2022; Kilpatrick et al. 2022), SN 2017jgh (Armstrong et al. 2021), and ZTF18aalrxas (Fremling et al. 2019). Additionally, interactions with

dense CSM around the progenitor star introduce complex shock structures (both forward and reverse), transforming kinetic energy into thermal radiation and significantly influencing the LC (e.g., Chevalier & Fransson 1994; Moriya et al. 2011). Energy diffusion from the densely packed ejecta also plays a role, especially in the early to mid-phases of the LC. These energy contributions, varying in their relative impact based on SN properties such as ^{56}Ni mass, CSM density, and explosion energy, collectively shape the unique LC signature of type I Ib SNe.

Type I Ib SNe progenitors are massive stars that have undergone substantial hydrogen envelope loss, resulting in a residual thin hydrogen layer at the explosion. This phenomenon occurs in two primary contexts: single massive stars, often exceeding $20 M_{\odot}$, where strong stellar winds or eruptions induced by nuclear burning phases precipitate significant hydrogen loss (Heger et al. 2003; Smith et al. 2011), and binary systems where a massive star transfers much of its hydrogen envelope to a companion, a process considered more prevalent and efficient for hydrogen stripping (Podsiadlowski et al. 1992; Eldridge et al. 2013). This binary interaction paradigm, responsible for many type I Ib SNe, aligns with observations and theoretical models (Maund et al. 2004; Fox et al. 2015), highlighting the diverse evolutionary pathways leading to these SNe. High-resolution imaging, notably from the Hubble Space Telescope, has identified diverse progenitors for SNe I Ib. Studies have revealed supergiants in binary systems for SNe I Ib 1993J (Maund & Smartt 2009) and 2001ig (Ryder et al. 2018), a stripped, Wolf-Rayet-like star for SN I Ib 2008ax (Crockett et al. 2008; Pastorello et al. 2008), and yellow supergiants for SNe I Ib 2011dh (Maund et al. 2011; Folatelli et al. 2014), 2013df (Maeda et al. 2015), and 2016gkg (Kilpatrick et al. 2022; Nayana et al. 2022), indicating a range of initial masses and binary interactions.

Bumpy LCs, marked by noticeable fluctuations in brightness over time, are a relatively common feature in certain types of SNe, particularly in superluminous SNe and type I In SNe. Recent research has shown that the LCs of hydrogen-poor superluminous SNe, which were thought to be powered by magnetar central engines, do not always follow the smooth decline predicted by a simple magnetar spin-down model (Hosseinzadeh et al. 2022). Hosseinzadeh et al. (2022) systematic study of 34 superluminous supernovae (SLSNe) revealed that the majority of these events cannot be explained solely by the smooth magnetar model, and they exhibit irregular bumps in their post-peak LCs. The cause of these bumps could be intrinsic to the SN (e.g., a variable central engine) or extrinsic (e.g., circumstellar interaction).

Some SNe I In, such as SN 2005la (Pastorello et al. 2008), SN 2006jd (Stritzinger et al. 2012), SN 2009ip (Margutti et al. 2014; Martin et al. 2015), and iPTF13z (Nyholm et al. 2017), display varied re-brightening episodes after peak brightness, ranging from short, early bumps to long, late ones. These irregularities in the LC are thought to arise from complex interactions between the SN ejecta and the circumstellar material. However, in the context of type I Ib SNe, the occurrence of bumpy LCs is notably rare, with no well-documented cases in the existing I Ib SN sample.

In this paper, we present follow-up observations and studies of the type I Ib SN SN 2019tua, which exhibits multiple bumps in its LCs. In Section 2, we summarize the observations of SN 2019tua. In Section 3, we analyze the observations and the properties of LCs and spectra, and includes a blackbody fitting of the spectral energy distribution. In Section 4, We described some simple physical LC models, and then used these models to fit the bolometric LC and relevant parameters. Our discussion and conclusions can be found in Section 5.

2. OBSERVATIONS AND DATA REDUCTION

2.1. Optical Photometry

SN 2019tua was discovered on October 31, 2019, at 07:52:19 UT (MJD = 58787.33) by Tonry et al. 2019, using the Asteroid Terrestrial-impact Last Alert System (ATLAS; Tonry et al. 2018) with the ATLAS-02 telescope at the Haleakala Observatory (Smith et al. 2021).

Its initial brightness, as filtered through the *cyan*, registered at a magnitude of 18.63 from the forced photometry obtained from the ATLAS forced-photometry server (Srivastav et al. 2019). It was first detected with *cyan* = 18.63 ± 0.139 at R.A. $21^{\text{h}}58^{\text{m}}00^{\text{s}}.280$ and Dec. $+24^{\circ}15'57''.10$. However, before the detection of SN 2019tua by ATLAS, the most recent observation of the same region by ATLAS was on October 29, 2019, at 07:09:07 (MJD = 58785.30), put a limit of brightness in the *orange* exceeding 19.49 (Srivastav et al. 2019). Thus, an explosion date (T_0) of 2019 October 29, at 07:09:07 UT (MJD = 58785.30) ± 2.0 days is adopted for the remainder of this work. The error listed on the explosion date is a flat distribution without any obvious bias toward the last nondetection or discovery. And it was also monitored by the Panoramic Survey Telescope and Rapid Response System (Pan-STARRS; Chambers et al. 2016). There is a first detection with Pan-STARRS on October 31, 2019, at 07:01:55 UT, 0.01 days before the first detection in *cyan*, and put a brightness of $w = 18.78$ mag.

Table 1. Optical Photometry of SN 2019tua

UT Date	Time	<i>B</i>	<i>V</i>	<i>R</i>	<i>I</i>	Telescope
	(days)	(mag)	(mag)	(mag)	(mag)	
2019-11-03	5.26	17.37±0.07	16.66±0.06	16.62±0.06	16.48±0.09	GWAC F60B
2019-11-06	8.13	17.02±0.08	16.16±0.07	16.10±0.07	15.75±0.10	GWAC F60B
2019-11-07	9.10	16.87±0.07	15.94±0.08	15.82±0.06	15.18±0.09	GWAC F60B
2019-11-08	10.09	16.79±0.06	15.84±0.06	15.64±0.08	15.35±0.08	GWAC F60B
2019-11-10	12.12	16.73±0.06	15.80±0.07	15.66±0.06	15.08±0.07	GWAC F60B
2019-11-14	16.14	16.21±0.08	15.35±0.08	15.16±0.06	14.64±0.07	GWAC F60B
2019-11-18	20.13	16.35±0.06	...	15.12±0.06	14.56±0.06	GWAC F60B
2019-11-19	21.14	16.37±0.05	15.36±0.08	15.09±0.06	...	GWAC F60B
2019-11-24	26.22	16.46±0.06	15.32±0.05	14.92±0.06	14.46±0.08	GWAC F60B
2019-11-25	27.26	16.46±0.10	15.37±0.04	14.96±0.07	...	GWAC F60B
2019-11-27	29.08	16.46±0.05	15.36±0.05	15.05±0.06	14.51±0.06	GWAC F60B
2019-11-28	30.17	16.69±0.06	15.45±0.05	15.10±0.06	14.46±0.09	GWAC F60B
2019-12-01	33.09	16.81±0.06	15.60±0.04	15.18±0.06	14.64±0.08	GWAC F60B
2019-12-03	35.27	16.92±0.09	15.64±0.04	15.22±0.07	...	GWAC F60B
2019-12-05	37.09	16.96±0.06	15.70±0.05	15.23±0.03	14.64±0.05	GWAC F60B
2019-12-06	38.09	17.11±0.07	15.78±0.04	15.29±0.06	14.68±0.08	GWAC F60B
2019-12-07	39.08	16.96±0.07	15.74±0.04	15.30±0.06	14.65±0.08	GWAC F60B
2019-12-08	40.14	17.01±0.13	15.70±0.09	15.31±0.08	...	GWAC F60B
2019-12-09	41.17	17.29±0.07	15.85±0.05	...	14.75±0.04	GWAC F60B
2019-12-10	42.08	17.54±0.07	15.88±0.04	15.35±0.06	14.75±0.06	GWAC F60B
2019-12-11	43.08	17.77±0.07	15.90±0.04	15.32±0.08	14.73±0.08	GWAC F60B
2019-12-12	44.08	17.36±0.09	15.86±0.06	15.32±0.06	14.66±0.03	GWAC F60B
2019-12-13	45.08	17.36±0.07	15.99±0.04	15.41±0.06	14.74±0.04	GWAC F60B
2019-12-17	49.10	17.21±0.05	15.83±0.04	15.33±0.07	14.81±0.05	GWAC F60B
2019-12-19	51.08	17.34±0.12	15.83±0.08	15.52±0.06	15.01±0.09	GWAC F60A
2019-12-20	52.08	17.43±0.11	15.91±0.08	15.71±0.09	15.17±0.05	GWAC F60A
2019-12-22	54.09	17.57±0.08	15.95±0.09	15.77±0.09	15.11±0.06	GWAC F60A
2019-12-28	60.10	17.56±0.09	16.16±0.09	15.73±0.05	14.95±0.07	GWAC F60B
2019-12-31	63.12	...	16.17±0.07	15.85±0.07	15.11±0.07	GWAC F60A
2020-01-01	64.11	15.90±0.08	15.19±0.08	GWAC F60A
2020-01-04	67.11	16.07±0.08	15.57±0.07	GWAC F60A
2020-01-20	83.11	16.40±0.08	15.74±0.05	GWAC F60A

NOTE—The GWAC F60A and F60B telescope photometry in *BVRI* bands. All photometry was corrected for the Galactic extinction. The time is relative to the reference time T_0 (MJD = 58785.30).

The SN 2019tua was observed in the *BVRI* bands using the Ground-based Wide Angle Camera (GWAC) F60A and F60B telescope at the Xinglong Observatory of National Astronomical Observatories (Xu et al. 2020). The *BVRI* bands images obtained from the first observation with the F60B telescope are shown in Figure 1. Our optical observations began 5.26 days after T_0 . The *B*-band observations of SN 2019tua extended for 55 days before the object became too faint for further observa-

tion, whereas the *BVI* optical bands were monitored for a span of 80 days, and several images were taken during each night, with an individual exposure time of 150 s frame. We combined multiple 150 s exposures obtained from observations for subsequent photometric processing. And the flat-field images were taken at dusk or dawn, while the bias images were taken at the beginning and the end of each observation.

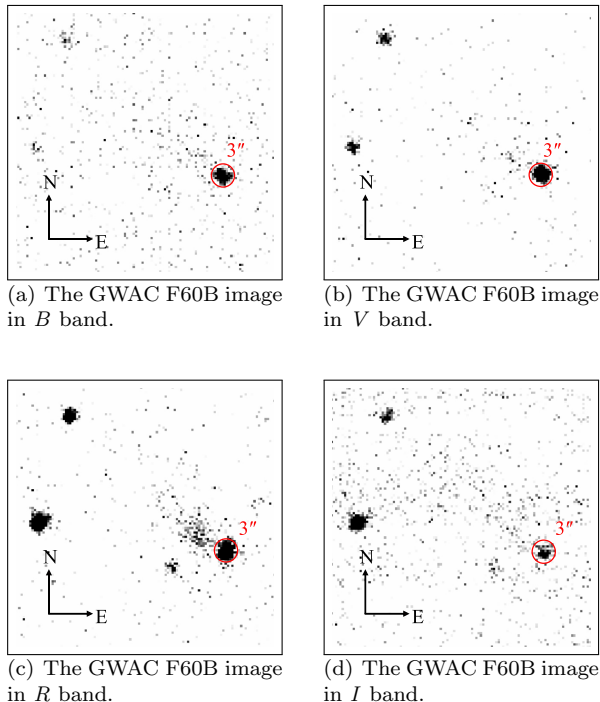


Figure 1. The *BVRI* bands images of the SN 2019tua obtained by the GWAC F60B telescope during its first observation on November 3, 2019, at 14:16:41.60 UT. These *BVRI* band images are obtained by combining three 150 s exposures each. The localization of the SN 2019tua is marked with a red circle in each panel, with a diameter of 3 arcseconds.

Photometric data processing was performed the aperture photometry, with the *apphot* task from the *IRAF* (Tody 1986). Photometric calibration was performed using the USNO B1.0 (Monet et al. 2003) and NOMAD (Zacharias et al. 2004) catalogs and the results are reported in Table 1 and the processed optical LCs are shown in Figure 2. Moreover, these photometric data were corrected for Galactic extinction correction with $E(B - V)_{\text{MW}} = 0.06$ (Schlafly & Finkbeiner 2011).

Additional observations of SN 2019tua were obtained in the *cyan* and *orange* filters in the ATLAS survey, the *w* and *i* filters with the Pan-STARRS system on the Pan-STARRS1 (PS1) telescope and Pan-STARRS2 (PS2) telescope, the *G* filter on the Gaia’s photometric instrument by the Gaia Science Alerts Project (Breedt 2019). And the *cyan*, *orange*, *w*, *i* and *G* forced-photometry light curves are shown in Figure 2, respectively.

2.2. Optical Spectroscopy

We obtained an optical spectrum of SN 2019tua by using the Beijing Faint Object Spectrograph and Camera (BFOSC) on the Xinglong 2.16m telescope at the

Xinglong Observatory of National Astronomical Observatories on November 27, 2019, at 18:39:43 UT (MJD = 58814.78) (Fan et al. 2016). The exposure time is 30 min. With a slit width of 1.8 arcseconds oriented in the north-south direction, the spectral resolution is approximately 10 Å when grating G4 was used, which results in a wavelength coverage of 3850 Å to 8000 Å. Wavelength calibration was conducted by employing an iron-argon comparison lamp. After bias subtraction and flat-field correction, we processed the two-dimensional spectrum via the *IRAF* package (Tody 1986). The isolated one-dimensional spectrum underwent wavelength and flux calibration through the corresponding comparison lamp and standard calibration star. Moreover, the spectrum was corrected for the redshift correction with $z = 0.010$ (Burke et al. 2019) and the Galactic extinction correction with $E(B - V)_{\text{MW}} = 0.06$ (Schlafly & Finkbeiner 2011). The resulting spectrum is shown in Figure 3.

We also included the spectrum that was uploaded to the Transient Name Serve (TNS¹) by (Burke et al. 2019) in our analysis, and it was observed by using the Folded Low Order whYte-pupil Double-dispersed Spectrograph (FLOYDS) on the 2 m Faulkes Telescope North (FTN) at Haleakala with a wavelength range of 3500 Å to 10000 Å (Brown et al. (2013)). And SN 2019tua exhibited a weak H α line in this early spectrum at day 3.3, which is consistent with typical type II Supernovae (Burke et al. 2019).

3. ANALYSIS

3.1. Light Curves Properties

The initial observation and the final non-detection, combined with a limiting magnitude of 19.73 in the *orange* band on the last day of non-detection (Tonry et al. 2019), argue against the likelihood of a pre-existing shock-cooling phase, such as those observed in SN 2008ax (Pastorello et al. 2008), SN 2011dh (Bersten et al. 2012), and SN 2020acat (Medler et al. 2022). Data from the *BVRI* bands, first collected approximately 5 days subsequent to the estimated date of explosion, also exhibit no deviation from a rapid luminosity increase, also negating the presence of extended shock-cooling emissions.

In Figure 2, SN 2019tua reached its optical peak around 25 days post-explosion, displaying a typical rise time for type IIb SN of 22.9 ± 0.8 days post-explosion (Taddia 2015). After reaching the peak, it exhibited significant bumps in the LC at around 40 - 50 days and 50 - 65 days. In this paper, the bumps we refer to are identi-

¹ www.wis-tns.org

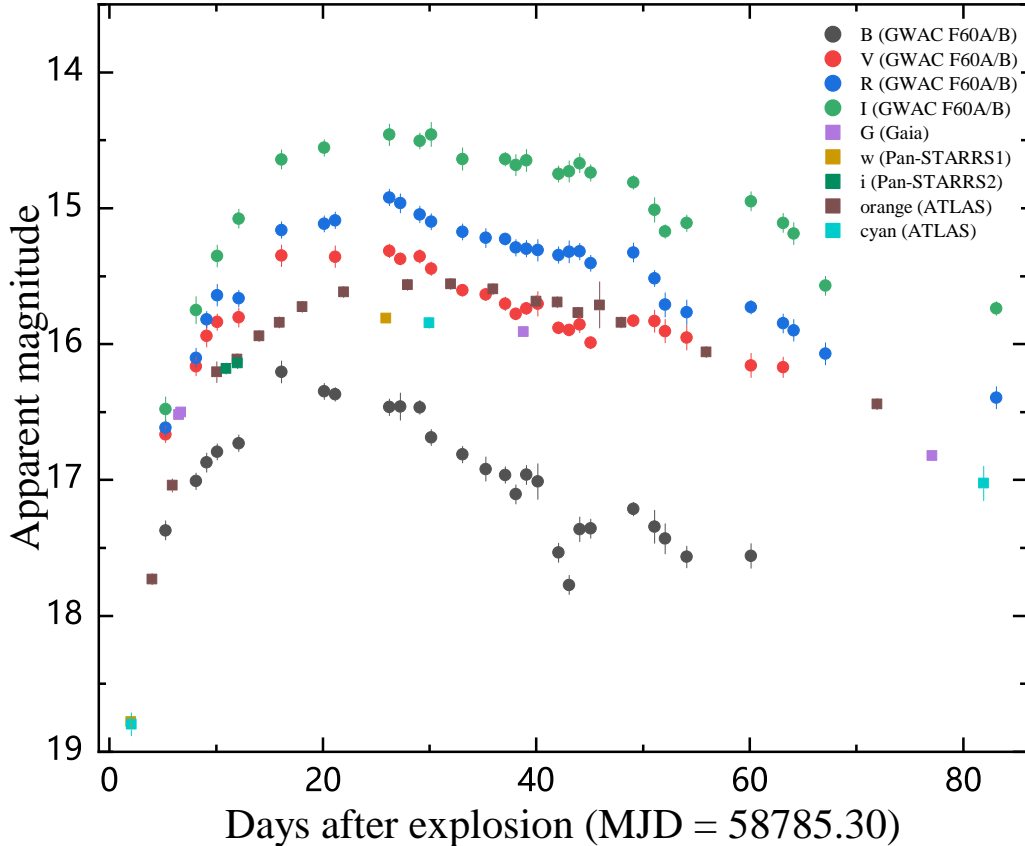


Figure 2. Multi-band LCs of SN 2019tua observed by GWAC F60A and F60B telescope are presented, with corrections for Galactic line-of-sight extinction. Our observations results are shown as circles, while squares markers represent data sourced from the TNS and some of other online report. Due to the dense data points from ATLAS, we binned and averaged the data taken within a single day, and then plotted these data.

fied through visual inspection. We designate as “bumps” the pronounced fluctuations in brightness occurring after the peak luminosity. Notably, there are conspicuous bumps both near and after the peak brightness of SN 2019tua. Our analysis only focuses on interpreting the bumps around 50 days post-explosion. The post-peak bump observed in SN 2019tua reminds the post-peak bump behavior seen in some of type II_b SNe, such as SN 2005la (Pastorello et al. 2008), SN 2006jd (Stritzinger et al. 2012), SN 2009ip (Margutti et al. 2014; Martin et al. 2015), and iPTF13z (Nyholm et al. 2017). These bumpy behaviors are typically attributed to interactions between SN ejecta and CSM (Liu et al. 2018; Andrews et al. 2019; Lin et al. 2023). Due to the brightness variation of SN 2019tua around 50 days post-explosion, We will explain these two bumps during the 40-50 and 50-65

days period post-explosion through model fitting in the Section 4.

3.2. Optical Spectral Properties

Figure 3 illustrates the spectral evolution of SN 2019tua from the rising phase ($t = 3.1$ days) to the peaking phase that 3.3 days after the peaking day ($t = 29.5$ days). In the subsequent spectrum at day 29.5, the $H\alpha$ line weakened, while the presence of multiple He absorption features justified its classification as a type II_b supernova. Our classification (type II_b) is differ from the Transient Name Server (TNS) classification (type II) and we will further discuss to demonstrate that our modification to the original classification. In order to further classify SN 2019tua, we compared its spectrum with the spectra of five similar-phase type II_b SNe (in Figure 4 and 5). These spectra were obtained from

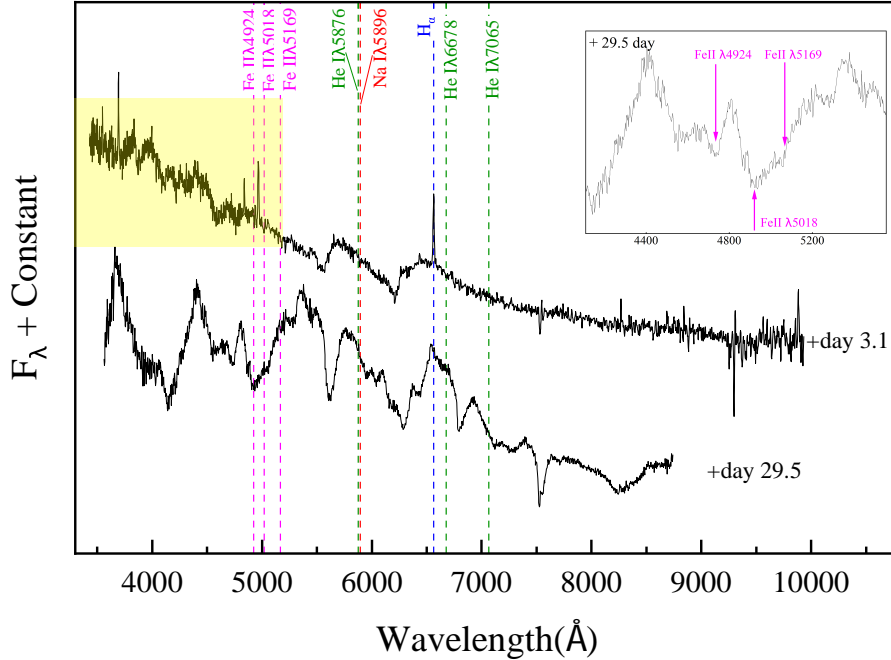


Figure 3. We obtained the spectrum of SN 2019tua using the Xinglong 2.16m telescope on day 29.5. For ease of analysis, we included the spectrum observed by the FTN telescope on day 3.3. And the lower spectrum in the figure is the spectrum observed by the Xinglong 2.16m telescope, while the upper one is the spectrum observed by the FTN telescope. The narrow emission lines within the yellow region may possibly originate from the host H II regions. The figure employs colored vertical lines to indicate the relevant Fe II, Na ID, He I, and H α lines. And the inset depicts the Fe II λ 4924, Fe II λ 5018 and Fe II λ 5169 lines that we have identified in the day 29.5 spectrum, and they are marked with purple arrows consistent with the main figure.

sne.space². We conducted a search for well-documented and renowned type IIb SNe during periods close to the observation times of the two key spectra of SN 2019tua (2.5-5.0 days and 25-35 days). The early spectrum of SN 2019tua at day 3.1 exhibits a prominent H α line, which is stronger compared to other IIb type SNe at similar phase, resembling the spectral features of SN 1996cb (Burke et al. 2019). The presence of strong hydrogen lines also associates SN 2019tua with other typical type II SNe. During this phase, in addition to the prominent, broad P-Cygni profile of the H α feature in its spectrum, the prominent broad feature of He I λ 5876 is also evident, indicating a thin hydrogen envelope for SN 2019tua prior to the explosion (Gutiérrez et al. 2014; Vallely et al. 2018). In the subsequent spectrum of SN 2019tua at 29.5 days, the H α line weakened and strong features of He I λ 5876, 6678, 7065 were observed. At this juncture, the He I λ 6678 emission line is broader than H α , and the H α P-Cygni absorption

feature is deeper than the He I λ 5876 absorption. This suggests that the He I λ 6678 feature is discernible within the emission component of the H α P-Cygni profile, indicating that H and He exist in distinct shells within SN 2019tua (Sahu et al. 2013; Medler et al. 2022). Furthermore, the spectrum of SN 2019tua at day 29.5 revealed a blueshifted “notched” between H α and He I λ 6678, which is also a useful signature for distinguishing SNe as type IIb SNe (Gal-Yam 2017). This feature is also evident in the spectra of other type IIb SNe at similar epochs, as shown in Figure 5. In summary, it is evident that SN 2019tua initially exhibited distinct hydrogen feature, with later develop strong He I lines (resembling SNe Ib), leading to its classification as a type IIb SN (Filippenko 1997; Gal-Yam 2017).

To estimate the reddening of the host galaxy, we searched for the interstellar absorption features of the Na ID lines in the corrected spectra. Figure 5 reveals no prominent, narrow Na ID absorption lines, implying that $E(B - V)_{\text{host}}$ is negligible. Although utilizing Na ID lines to estimate dust extinction is not entirely reliable—owing to the possibility that the absence

² <https://github.com/astrocatalogs/supernovae>

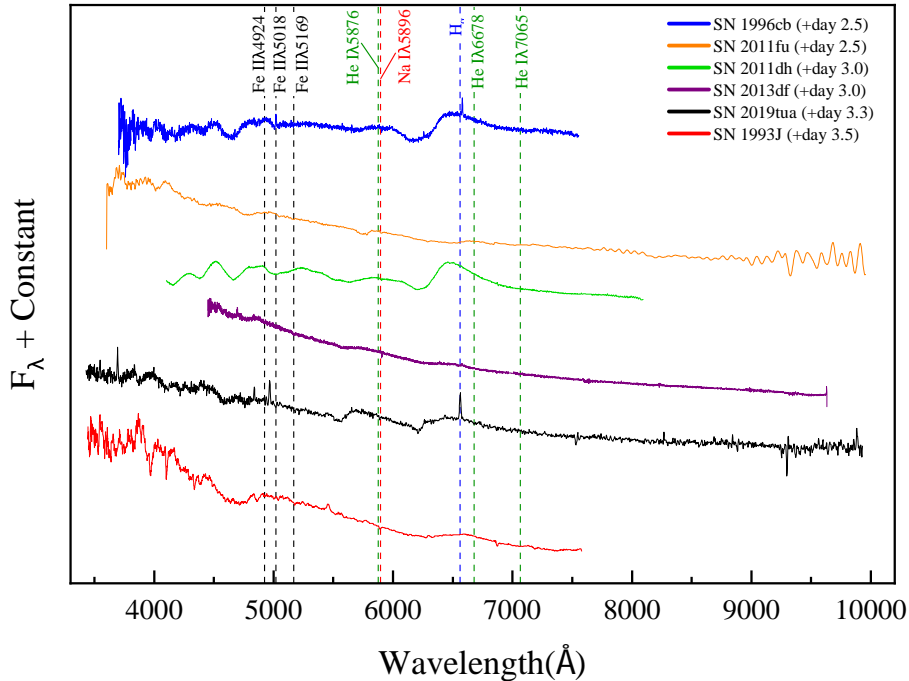


Figure 4. Early-time spectra of SN 2019tua compared with spectrum of other SNe I Ib. Phase from explosion date for individual SNe is given in the legend, and notable spectral features are identified with color vertical lines at their rest-frame wavelengths.

of Na ID lines could be attributed to the low resolution of the spectra (Poznanski et al. 2011)—the lack of detectable Na ID signatures typically suggests minimal reddening in the host galaxy (Phillips et al. 2013). Consequently, we infer that the extinction in the host galaxy UGC-11860 is negligible in comparison to the reddening caused by the Milky Way, the total reddening is solely attributed to Galactic sources, applying a correction of $E(B - V) = 0.06$ mag (Schlafly & Finkbeiner 2011).

Typically, the photospheric velocity of the SN is determined using the absorption linear velocities of Fe II lines at wavelengths 4924 Å, 5018 Å, and 5169 Å (Roy et al. 2016). During the spectrum of the peaking phase, the velocities for the three Fe II lines are found to be 3700 ± 500 km s⁻¹, 4900 ± 700 km s⁻¹, and 8100 ± 1200 km s⁻¹, respectively. The mean velocity, denoted as V_{phot} , is approximately 5600 km s⁻¹ at peak luminosity.

3.3. Bolometric Light Curve

Using *BVRI* photometry, we constructed the spectral energy distribution (SED) and quasi-bolometric LC of SN 2019tua, as well as the effective temperature and photospheric radius. Due to the limited of optical data, the error in the derived bolometric LC data of

SN 2019tua may be slightly larger compared to those derived from SNe with more bands. The fitting procedure for the bolometric LC employs the publicly accessible *Superbol* program (Mnicholl 2018).

After conducting reddening corrections on the collected data and adjusting for the distance modulus at $z = 0.010$, linear interpolation is executed on each band of the LC to supplement missing data points with corresponding observations in the *R* band. And then, spectral energy distributions (SEDs) are generated for each point on the LC using the *emcee* Python package (Foreman-Mackey et al. 2013). Each spectral energy distribution is then fitted with a blackbody function via the nonlinear least squares method, using the *curve-fit* function in *scipy* (Virtanen et al. 2020). The uncertainties are estimated using a Markov Chain Monte Carlo (MCMC) approach. We ran the MCMC with 600 steps. The results of the fitting are illustrated in Figure 6, and the best-fit parameters are enumerated in Table 2 and depicted in Figure 7. We employed the blackbody equation to fit the SEDs of SN 2019tua, thereby deriving the bolometric LC, as well as the temperature and radius evolution for each epoch of SN 2019tua.

Taking into account the observed excess in the *V* band within SN 2019tua’s SED, particularly in conjunction

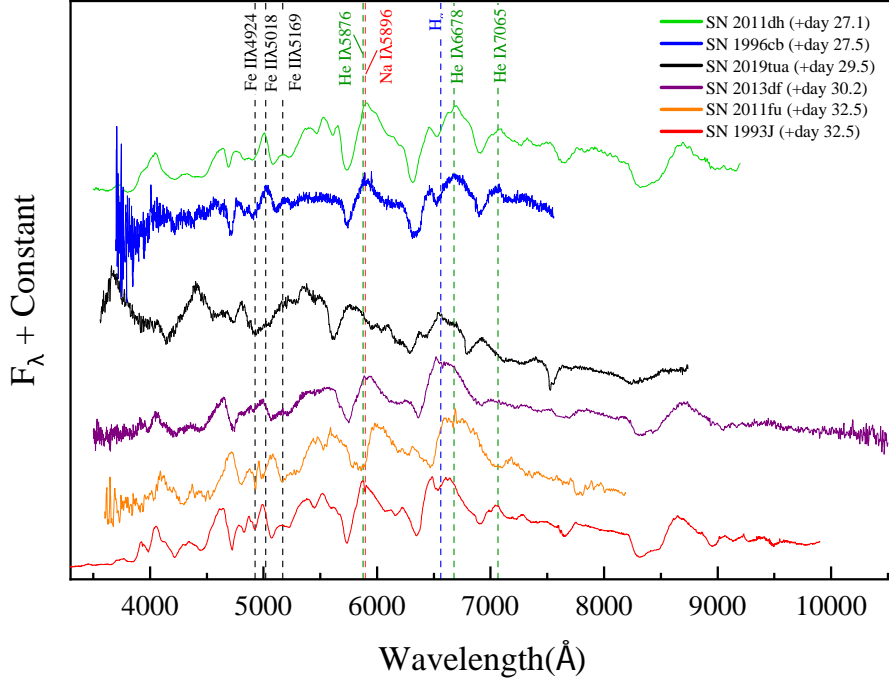


Figure 5. Comparison at about ~ 3 days post-peak of the spectrum of SN 2019tua with spectra of other SNe IIB. Phase from explosion date for individual SNe is given in the legend, and notable spectral features are identified with color vertical lines at their rest-frame wavelengths.

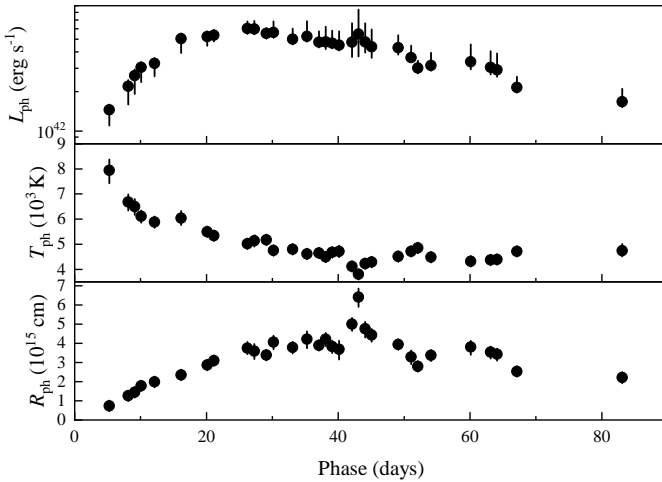


Figure 6. In addition to the main peak, it's very clear to see the bumps on the quasi-bolometric LC. Top panel: The bolometric LC of SN 2019tua, obtained by integrating the flux from the *BVRI* bands. Second panel: effective temperature. Bottom panel: photospheric radius.

with the time corresponding to the bump in the LCs in 2, a sustained excess is evident in the *V* band from approximately day 40 to day 65. It could be the presence of a transient additional energy source in the *V*

band. Such an ancillary radiation mechanisms could significantly contribute to the observed excess in this band (Yan et al. 2017; Nicholl et al. 2017). From Figure 2, the performance of the *B* band appears inconsistent when compared to other bands. Less pronounced fluctuations are observed in other bands than in the *B* band. These variations among the bands have implications for the quality of our SED fit, and subsequently influence the derived bolometric LC. We conducted observations of SN 2019tua across multiple bands from day 40 to day 55, during which a noticeable bump was evident in the quasi-bolometric LC. The secondary peak in the *B* band is more pronounced compared to other bands, as depicted in Figure 2. This situation may be the reason for the maximum error in SED fitting to occur at around 40 days, thereby amplifying the error of the bolometric LC at the same time.

We determined the peak time (t_{peak}) of SN 2019tua by directly selecting the period with the maximum luminosity value from Table 2, yielding $t_{\text{peak}} = 26.22 \pm 1.0$ days. Consequently, we obtained the peak luminosity L_{peak} of SN 2019tua is $6.07 \times 10^{42} \text{ erg s}^{-1}$, substantially exceeding the typical luminosity of SNe IIB and even surpassing the L_{peak} of some SNe Ib (Afsariardchi

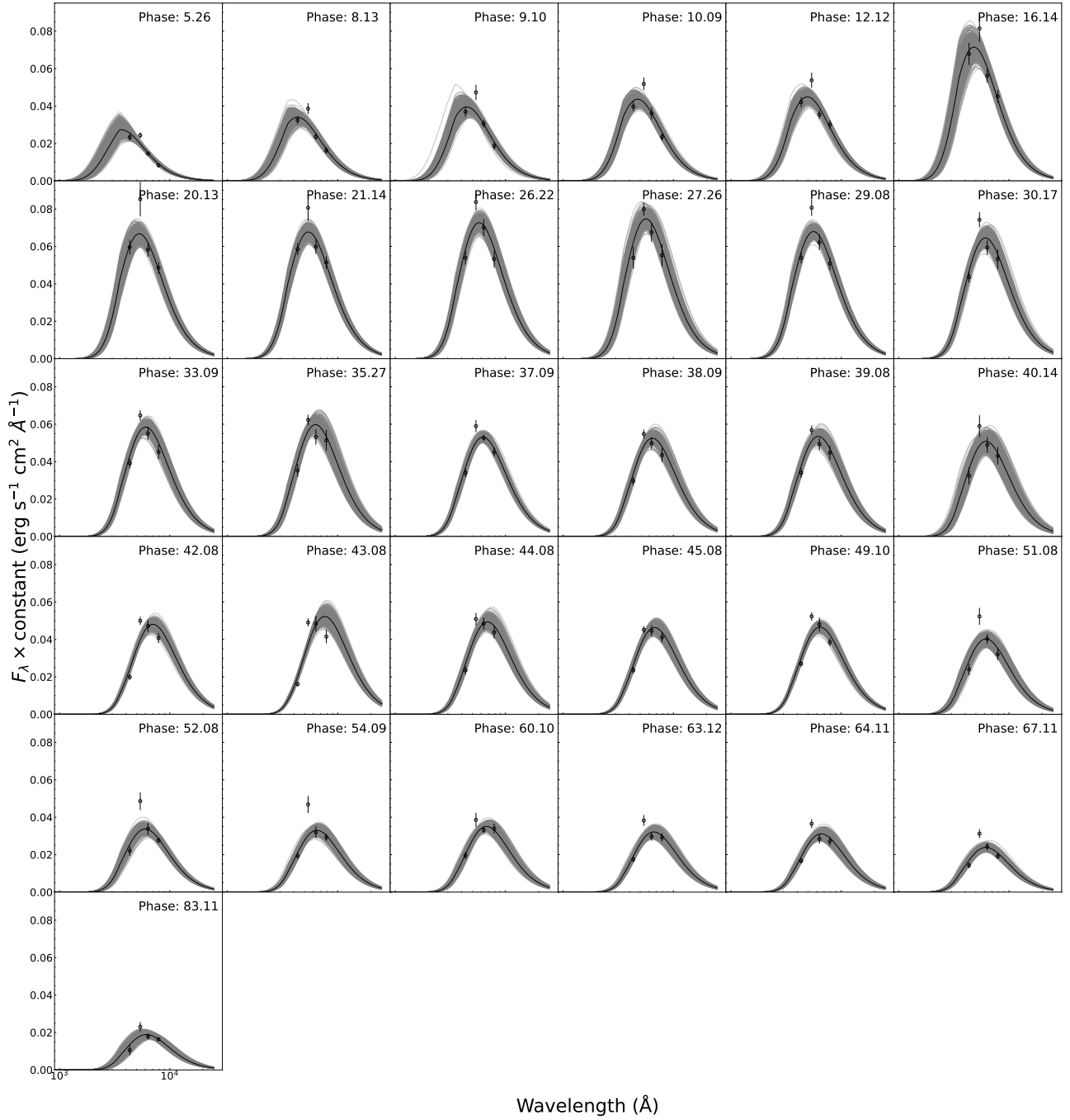


Figure 7. Blackbody fits to the *BVRI* photometry of SN 2019tua. During epochs with no observed in *BVI* bands, the optical data has been interpolated. An excess in the *V* band compared to the blackbody function was observed. The extracted samples are represented by the light gray lines, and the dispersion corresponds to the overall uncertainty in the fit. The black line represents the best fit line associated with the data points.

Table 2. Best-fit Parameters of the Blackbody Fits

Phase (days)	L_{ph} ($10^{42} \text{ erg s}^{-1}$)	T_{ph} (10^3 K)	R_{ph} (10^{15} cm)	χ^2/dof
5.26	$1.45^{+0.10}_{-0.35}$	$7.94^{+0.43}_{-0.31}$	$0.73^{+0.07}_{-0.07}$	5.50
8.13	$2.19^{+0.25}_{-0.60}$	$6.68^{+0.31}_{-0.34}$	$1.26^{+0.12}_{-0.13}$	4.41
9.10	$2.64^{+0.30}_{-0.72}$	$6.47^{+0.30}_{-0.33}$	$1.45^{+0.14}_{-0.15}$	4.48
10.09	$3.06^{+0.25}_{-0.70}$	$6.11^{+0.23}_{-0.26}$	$1.78^{+0.16}_{-0.16}$	5.64
12.12	$3.27^{+0.17}_{-0.66}$	$5.88^{+0.22}_{-0.23}$	$1.99^{+0.16}_{-0.18}$	4.33
16.14	$5.05^{+0.29}_{-1.13}$	$6.05^{+0.28}_{-0.28}$	$2.35^{+0.22}_{-0.25}$	2.30
20.13	$5.23^{+0.02}_{-0.78}$	$5.49^{+0.19}_{-0.18}$	$2.87^{+0.22}_{-0.24}$	2.52
21.14	$5.37^{+0.19}_{-0.56}$	$5.54^{+0.15}_{-0.16}$	$3.10^{+0.22}_{-0.24}$	2.35
26.22	$6.07^{+0.79}_{-0.25}$	$5.02^{+0.15}_{-0.17}$	$3.75^{+0.32}_{-0.32}$	4.94
27.26	$5.97^{+0.91}_{-0.41}$	$5.25^{+0.21}_{-0.23}$	$3.59^{+0.37}_{-0.41}$	2.89
29.08	$5.53^{+0.41}_{-0.33}$	$5.18^{+0.13}_{-0.14}$	$3.38^{+0.23}_{-0.24}$	5.50
30.17	$5.62^{+1.21}_{-0.15}$	$4.75^{+0.14}_{-0.15}$	$4.06^{+0.34}_{-0.37}$	6.12
33.09	$5.01^{+1.02}_{-0.17}$	$4.79^{+0.14}_{-0.13}$	$3.78^{+0.29}_{-0.31}$	6.62
35.27	$5.26^{+1.60}_{-0.33}$	$4.61^{+0.17}_{-0.17}$	$4.21^{+0.41}_{-0.47}$	5.14
37.09	$4.75^{+1.00}_{-0.34}$	$4.64^{+0.11}_{-0.11}$	$3.89^{+0.23}_{-0.25}$	4.77
38.09	$4.76^{+1.46}_{-0.55}$	$4.49^{+0.13}_{-0.12}$	$4.22^{+0.32}_{-0.37}$	6.36
39.09	$4.67^{+1.15}_{-0.27}$	$4.69^{+0.13}_{-0.15}$	$3.83^{+0.31}_{-0.34}$	4.80
40.14	$4.51^{+1.24}_{-0.05}$	$4.58^{+0.23}_{-0.23}$	$3.69^{+0.44}_{-0.53}$	2.08
42.08	$4.74^{+1.88}_{-1.07}$	$4.12^{+0.09}_{-0.09}$	$5.00^{+0.32}_{-0.35}$	17.67
43.08	$5.48^{+2.92}_{-1.79}$	$3.80^{+0.08}_{-0.08}$	$6.40^{+0.45}_{-0.50}$	24.22
44.08	$4.77^{+1.84}_{-0.82}$	$4.22^{+0.13}_{-0.12}$	$4.75^{+0.37}_{-0.45}$	4.92
45.08	$4.38^{+1.56}_{-0.77}$	$4.29^{+0.10}_{-0.11}$	$4.43^{+0.31}_{-0.35}$	4.66
49.10	$4.30^{+1.06}_{-0.48}$	$4.50^{+0.09}_{-0.09}$	$3.94^{+0.22}_{-0.24}$	12.41
51.08	$3.62^{+0.85}_{-0.01}$	$4.70^{+0.20}_{-0.19}$	$3.29^{+0.33}_{-0.38}$	6.24
52.08	$3.02^{+0.41}_{-0.11}$	$4.83^{+0.18}_{-0.17}$	$2.79^{+0.22}_{-0.26}$	6.49
54.09	$3.16^{+0.78}_{-0.19}$	$4.47^{+0.14}_{-0.13}$	$3.37^{+0.26}_{-0.03}$	7.19
60.10	$3.36^{+1.20}_{-0.42}$	$4.31^{+0.16}_{-0.14}$	$3.80^{+0.33}_{-0.41}$	2.59
63.12	$3.05^{+1.00}_{-0.36}$	$4.36^{+0.14}_{-0.12}$	$3.54^{+0.29}_{-0.34}$	6.54
64.11	$2.92^{+0.97}_{-0.33}$	$4.39^{+0.13}_{-0.14}$	$3.43^{+0.29}_{-0.34}$	8.37
67.11	$2.15^{+0.44}_{-0.01}$	$4.71^{+0.16}_{-0.16}$	$2.53^{+0.22}_{-0.24}$	8.46
83.11	$1.67^{+0.43}_{-0.01}$	$4.52^{+0.27}_{-0.23}$	$2.43^{+0.23}_{-0.30}$	2.72

et al. 2021) (in Figure 8). And the bolometric LC of SN 2019tua is consistent with the general trend illustrated in Figure 2. Those bolometric LCs were obtained from sne.space and used the same method as described in the (Afsariardchi et al. 2021), and the explosion times used were also derived from (Afsariardchi et al. 2021).

Additionally, SN 2019tua exhibits higher luminosity compared to some other type IIb SNe, such as SN 2010as $\sim 2.7 \times 10^{42} \text{ erg s}^{-1}$ (Folatelli et al. 2014), SN 2020acat $\sim 3.1 \times 10^{42} \text{ erg s}^{-1}$ (Medler et al. 2022; Ergon et al.

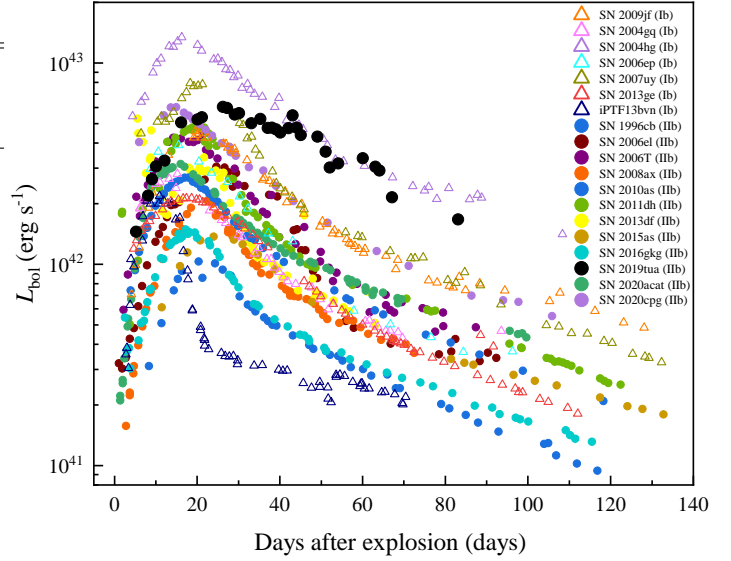


Figure 8. Bolometric light curves of SN 2019tua in comparison with some of other type IIb and type Ib SNe. Type IIb SNe are shown as circles, while hollow triangular markers represent type Ib SNe.

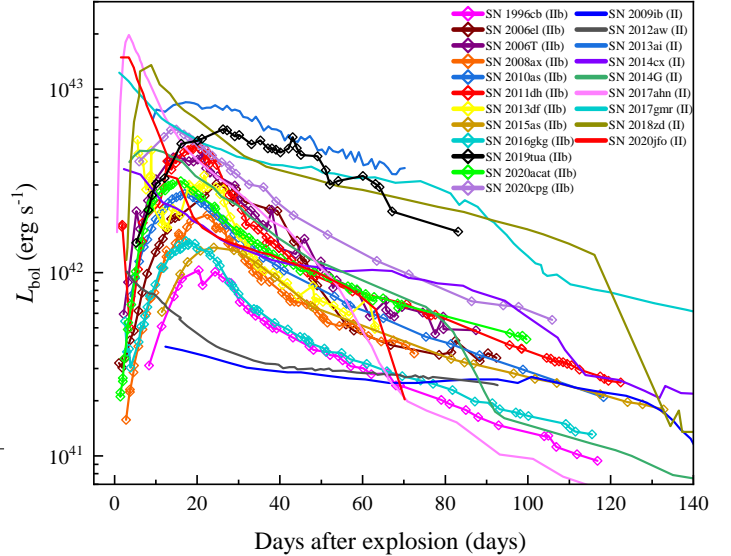


Figure 9. Bolometric light curves of SN 2019tua and some type IIb SNe in comparison with some of other type II SNe. Type IIb SNe are shown by colored hollow rhombus connected by colored solid lines and the other type II SNe are shown by colored solid lines.

2024), SN 2015as $\sim 5.2 \times 10^{42} \text{ erg s}^{-1}$ (Gangopadhyay 2018). And the L_{peak} of SN 2019tua is similar to SN 2020cpg $\sim 6.03 \times 10^{42} \text{ erg s}^{-1}$ (Medler et al. 2021; Teffs et al. 2022). We also plotted the LCs from the reference (Folatelli et al. 2014; Medler et al. 2022; Teffs et al. 2022; Gangopadhyay 2018) as shown in Figure 8, with the

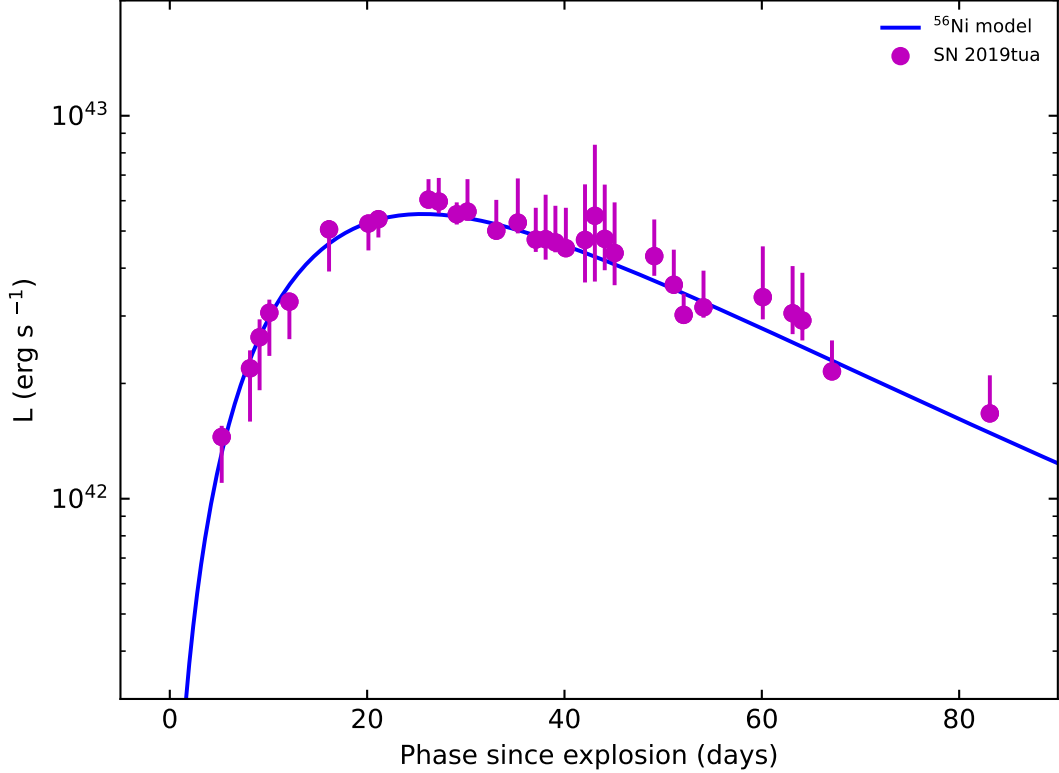


Figure 10. The bolometric LC of SN 2019tua reproduced by the ^{56}Ni model. The total luminosity $L_{\text{inp,Ni}}$ is represented by the solid blue line.

Table 3. Parament of the ^{56}Ni Model

M_{ej}	M_{Ni}	κ	$\kappa_{\gamma,\text{Ni}}$	t_{expl}	χ^2/dof	AIC	BIC
(M_{\odot})	(M_{\odot})	($\text{cm}^2 \text{g}^{-1}$)	($\text{cm}^2 \text{g}^{-1}$)	(days)			
$1.38^{+0.99}_{-0.57}$	$0.38^{+0.03}_{-0.02}$	$0.19^{+0.13}_{-0.08}$	$0.01^{+0.01}_{-0.00}$	$-1.05^{+0.80}_{-0.87}$	0.37	19.65	55.70

NOTE—The uncertainties are 1σ .

aligned the explosion time. In contrast, the luminosity of SN 2019tua is lower than the type IIb, such as SN 2018gk $\sim 7.0 \times 10^{43} \text{ erg s}^{-1}$ (Bose et al. 2021).

In addition, we further attempted to compare the bolometric LCs of SN 2019tua and some type IIb SNe with those of other well-documented type II SNe, such as SN 2009ib (Takáts et al. 2015), SN 2012aw (Yadav et al. 2014), SN 2013ai (Davis et al. 2021), SN 2014G (Terreran et al. 2016), SN 2014cx (Huang et al. 2016), SN 2017ahn (Tartaglia et al. 2021), SN2017gmr (Andrews et al. 2019), SN 2018zd (Zhang et al. 2020), SN 2022jfo (Teja et al. 2022). The results are presented in

Figure 9 and we also plotted these LCs from the reference with the aligned the explosion time, respectively. It can be clearly observed that, compared to type II SNe, type IIb SNe generally take a longer time to rise to their peak luminosities. The type II SNe typically reach peak luminosity within one to two weeks, whereas type IIb SNe require more time (Pessi et al. 2019). Additionally, the late-time luminosity decline of type IIb SNe is noticeably slower compared to type II-L SNe but faster than type II-P SNe and the different decline rates were proposed to correlate with the amount of hydrogen retained by the progenitor (Davis et al. 2021). It has been

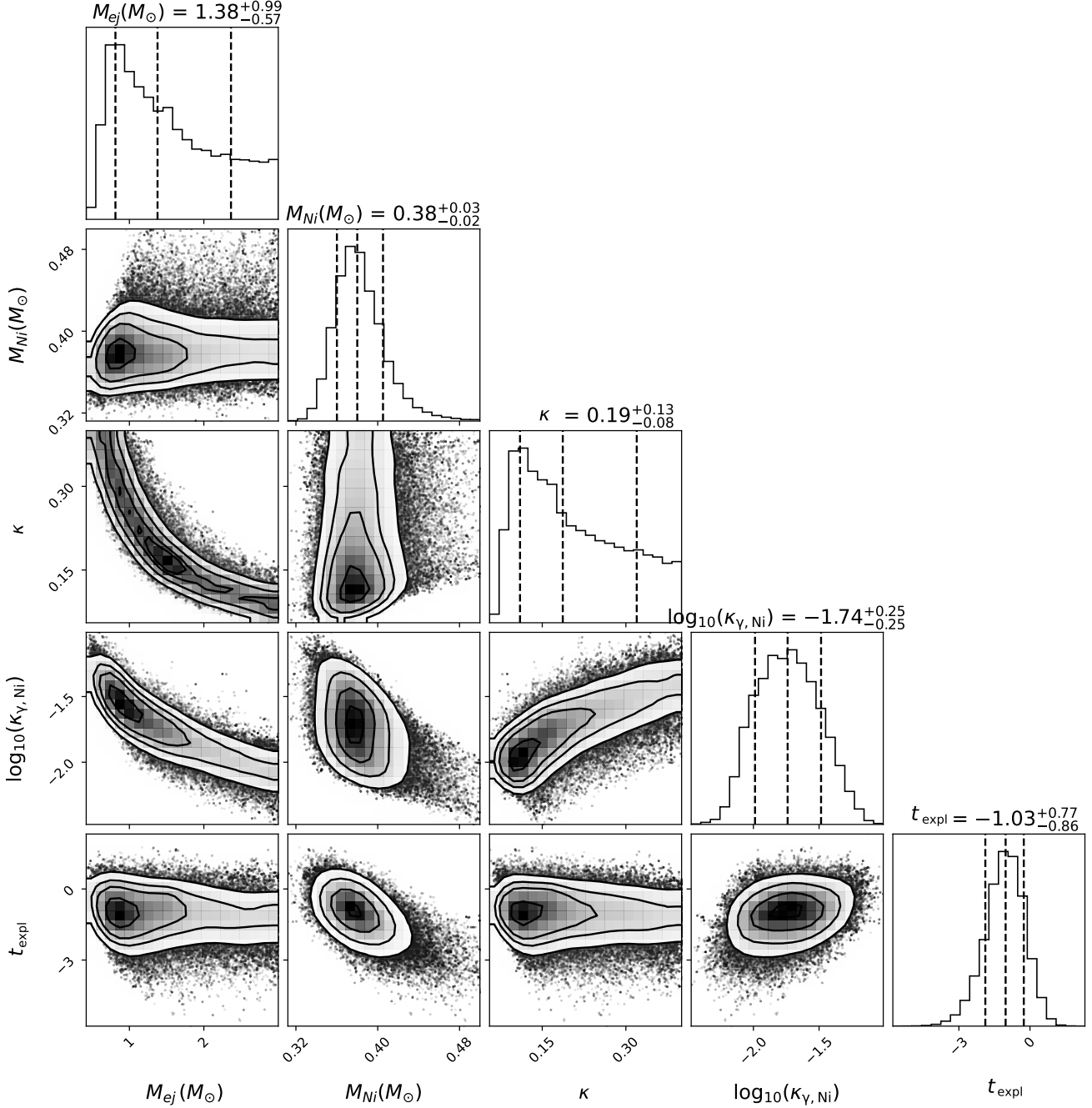


Figure 11. The corner plot for the ^{56}Ni model. The uncertainties are computed as the 16th and 84th percentiles (1σ) of the posterior samples along each axis.

claimed that type Ib, IIb, II-L, and type II-P SNe all result from the collapse of massive stars, with their main differences depending on the details of the mass loss and the amount of mixing (Davis et al. 2021).

4. MODELLING OF SN 2019TUA

In this section, we apply four distinct energy source models to fit the bolometric LC of SN 2019tua: the ^{56}Ni model, the ejecta-circumstellar medium interaction (CSI) model, the magnetar model, and the combined CSI plus ^{56}Ni model. We restrict our focus to dense shell CSM models with $s = 0$. To identify the optimal fit parameters, we employ Bayesian analysis using the *emcee* Python package (Foreman-Mackey et al. 2013), which is based on MCMC techniques. Maximum likeli-

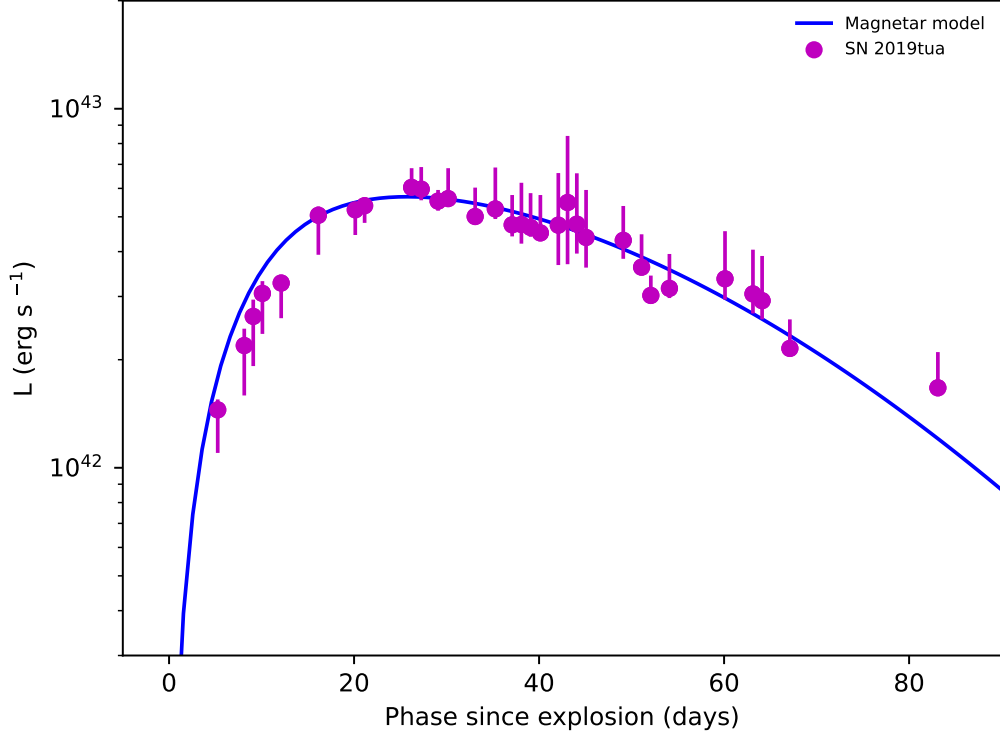


Figure 12. The bolometric LC of SN 2019tua reproduced by the magnetar model. The total luminosity $L_{\text{inp,mag}}$ is represented by the solid blue line.

Table 4. Parament of the Magnetar Model

M_{ej}	P_{NS}	κ	B	$\kappa_{\gamma,\text{mag}}$	t_{expl}	χ^2/dof	AIC	BIC
(M_{\odot})	(ms)	($\text{cm}^2 \text{g}^{-1}$)	(10^{14}G)	($\text{cm}^2 \text{g}^{-1}$)	(days)			
$3.81^{+2.51}_{-1.68}$	$9.66^{+0.98}_{-0.87}$	$0.39^{+0.30}_{-0.16}$	$9.50^{+2.81}_{-2.58}$	$0.01^{+0.00}_{-0.01}$	$-0.47^{+1.28}_{-0.94}$	0.98	36.45	79.71

NOTE—The uncertainties are 1σ .

hood χ^2 fitting is performed, and posterior probability distributions for the free parameters are provided. To assess the quality of the fits, we conduct Akaike and Bayesian Information Criterion (AIC/BIC) tests. Details of free parameters and their prior conditions for each model are elaborated in the respective tables. Simulations are executed with 100,000 steps, and the fitting uncertainty is quantified within a 1σ confidence interval.

In the case of a homogeneously expanding photosphere with energy injection concentrated at the center, the observed bolometric luminosity can be expressed as follows (Arnett 1982; Chatzopoulos et al. 2012):

$$L_{\text{bolo}}(t) = \frac{2}{\tau_m} e^{-\frac{t^2}{\tau_m^2}} \int_0^t e^{\frac{t'^2}{\tau_m^2}} \frac{t'}{\tau_m} L_{\text{inp}}(t') dt', \quad (1)$$

where $L_{\text{inp}}(t')$ is the input luminosity, $\tau_m = \left(\frac{10\kappa M_{\text{ej}}}{3\beta v c}\right)^{1/2}$ is the effective LC timescale, κ is the gray opacity, and $\beta \simeq 13.4$ is a dimensionless constant related to the geometry of the ejecta. The ejecta velocity is set to $v = 5600 \text{ km s}^{-1}$ based on the velocities of the Fe II lines derived in the previous section.

4.1. The ^{56}Ni Model

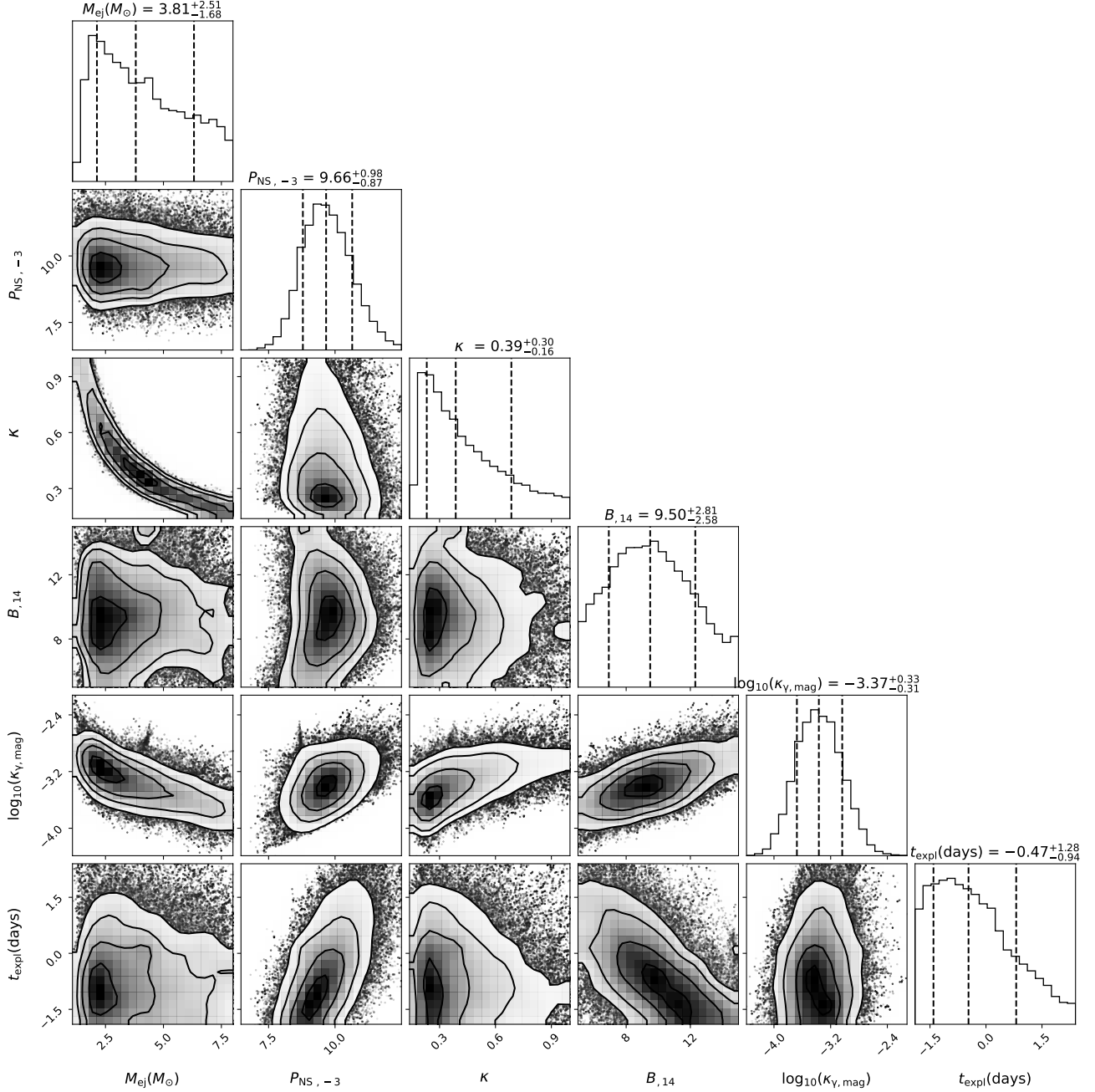


Figure 13. The corner plot for the magnetar model. The uncertainties are computed as the 16th and 84th percentiles (1σ) of the posterior samples along each axis.

The input luminosity produced by the decay chain $^{56}\text{Ni} \rightarrow ^{56}\text{Co} \rightarrow ^{56}\text{Fe}$ can be written as (Colgate & McKee 1969; Colgate et al. 1980; Arnett 1980, 1982):

$$L_{\text{inp,Ni}}(t) = M_{\text{Ni}} \times \left[(\epsilon_{\text{Ni}} - \epsilon_{\text{Co}}) e^{-t/\tau_{\text{Ni}}} + \epsilon_{\text{Co}} e^{-t/\tau_{\text{Co}}} \right] (1 - e^{-\tau_{\gamma,\text{Ni}}}), \quad (2)$$

where M_{Ni} is the mass of ^{56}Ni . $\epsilon_{\text{Ni}} = 3.9 \times 10^{10} \text{ erg g}^{-1} \text{ s}^{-1}$ and $\epsilon_{\text{Co}} = 6.78 \times 10^9 \text{ erg g}^{-1} \text{ s}^{-1}$. $\tau_{\text{Ni}} = 8.8 \text{ days}$ and $\tau_{\text{Co}} = 111.3 \text{ days}$ are the decay time

of ^{56}Ni decays to ^{56}Co and ^{56}Co decays to ^{56}Fe , respectively. $\tau_{\gamma,\text{Ni}}$ is the optical depth of the ejecta to gamma-rays and can be written as $\tau_{\gamma,\text{Ni}} = 3\kappa_{\gamma,\text{Ni}} M_{\text{ej}} / 4\pi R_{\text{ej}}^2$.

The ^{56}Ni model has five free parameters: the optical opacity κ ($\text{cm}^2 \text{ g}^{-1}$), the ejecta mass M_{ej} (M_{\odot}), the ^{56}Ni mass M_{Ni} (M_{\odot}), the gamma-ray opacity of ^{56}Ni decay photons κ_{γ} ($\text{cm}^2 \text{ g}^{-1}$), and the epoch of the explosion t_{expl} (days). The fitting results are illustrated in Figure

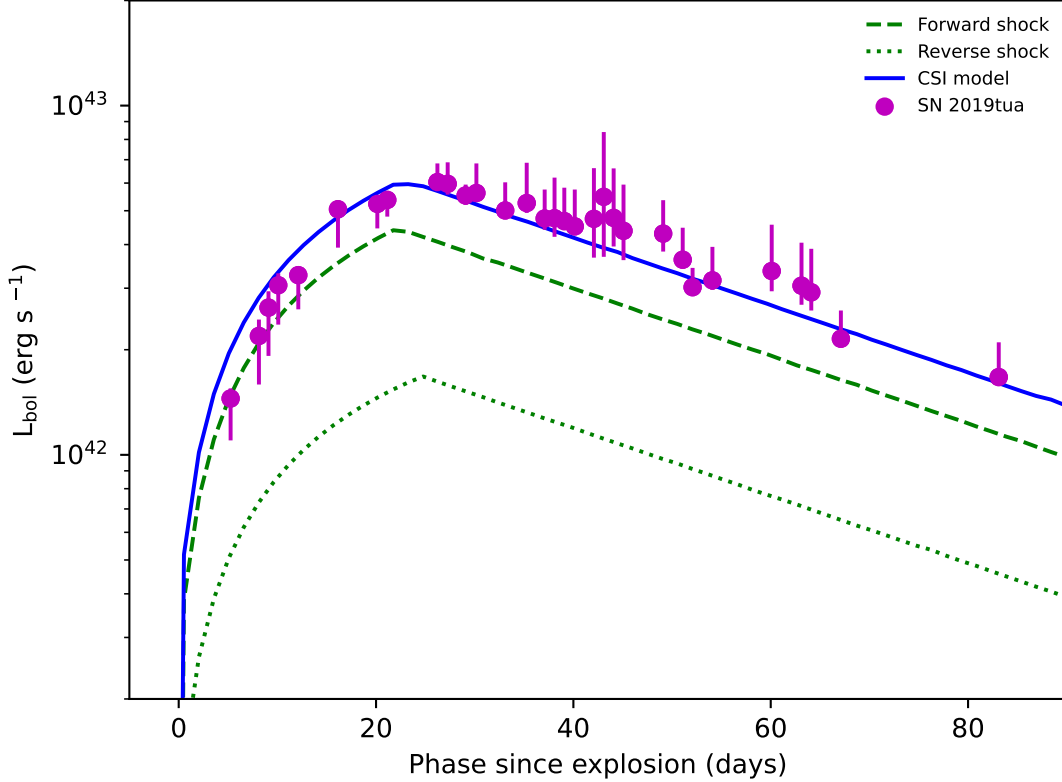


Figure 14. The bolometric LC of SN 2019tua reproduced by the CSI model. The total luminosity L_{CSI} is represented by the solid blue line, the contribution of the forward shock $L_{\text{inp,FS}}$ is shown by the green dashed line, and the contribution of the reverse shock $L_{\text{inp,RS}}$ is shown by the green dotted line.

Table 5. Parament of the CSI Model

M_{ej}	M_{CSM}	κ	ρ_{CSM}	$R_{\text{CSM,in}}$	ϵ	x_0	t_{expl}	χ^2/dof	AIC	BIC
(M_{\odot})	(M_{\odot})	($\text{cm}^2 \text{g}^{-1}$)	($10^{-12} \text{g cm}^{-3}$)	(10^{14}cm)			(days)			
$2.44^{+1.76}_{-1.20}$	$4.19^{+1.04}_{-1.07}$	$0.25^{+0.10}_{-0.11}$	$28.83^{+10.91}_{-11.38}$	$14.02^{+6.00}_{-6.10}$	$0.50^{+0.20}_{-0.16}$	$0.34^{+0.07}_{-0.05}$	$-0.98^{+0.94}_{-0.87}$	0.35	23.98	81.66

NOTE—The uncertainties are 1σ .

10 and summarized in Table 3. The corner plots of the ^{56}Ni model are shown in Figure 11.

4.2. The Magnetar Model

The magnetar model accounts for the LC of SNe by converting the rotational energy of a newborn magnetar—originating from the collapse of a massive star—into the thermal energy of the SN ejecta. The input power generated through magnetic dipole radiation

can be described by

$$L_{\text{inp,mag}}(t) = \frac{E_p}{\tau_p} \frac{1}{(1 + t/\tau_p)^2} \left(1 - e^{-At^{-2}}\right), \quad (3)$$

where $E_p \simeq (1/2)I_{\text{NS}}\Omega^2$ is the rotational energy of a magnetar, $\tau_p = 6I_{\text{NS}}c^3/B^2R_{\text{NS}}^6\Omega^2$ is the spin-down timescale of the magnetar, $I_{\text{NS}} = (2/5)M_{\text{NS}}R_{\text{NS}}^2$ is the moment of inertia of a magnetar (Kasen & Bildsten 2010). $M_{\text{NS}} = 1.4 M_{\odot}$, $R_{\text{NS}} = 10 \text{ km}$ and $P = 2\pi/\Omega$ are the mass, radius and rotational period of the magnetar, respectively. A trapping factor $1 - e^{-At^{-2}}$ is introduced

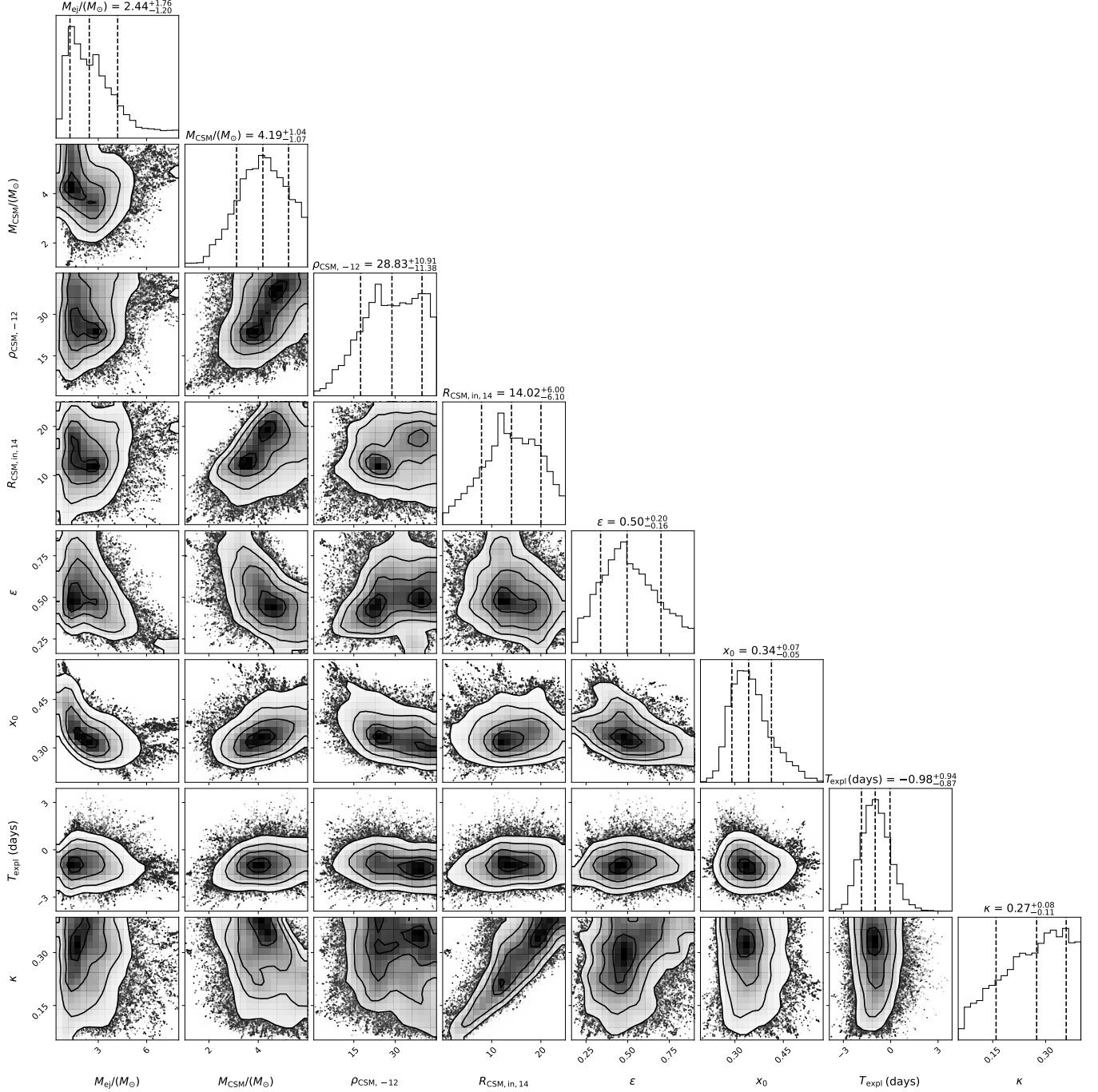


Figure 15. The corner plot for the CSI model ($s = 0$). The uncertainties are computed as the 16th and 84th percentiles (1σ) of the posterior samples along each axis.

in the magnetar-powered model to represent gamma/X-ray leakage and trapping rate (Wang et al. 2015), where A can be written as $A = \frac{3\kappa_{\gamma,\text{mag}}M_{\text{ej}}}{4\pi v^2}$.

In the magnetar model, we consider six free parameters for fitting: the ejected mass M_{ej} (M_{\odot}), the initial spin period of the magnetar P_{NS} (ms), the optical opacity κ ($\text{cm}^2 \text{g}^{-1}$), the magnetic field strength B (10^{14} G), the gamma-ray opacity for photons generated by mag-

netar spin-down $\kappa_{\gamma,\text{mag}}$ ($\text{cm}^2 \text{g}^{-1}$), and the explosion time t_{expl} (days). The theoretical bolometric LC fitted using the magnetar model is depicted in Figure 12, and the best-fit parameters are listed in Table 4. The corner plots of the magnetar model are shown in Figure 13.

4.3. The CSI Model

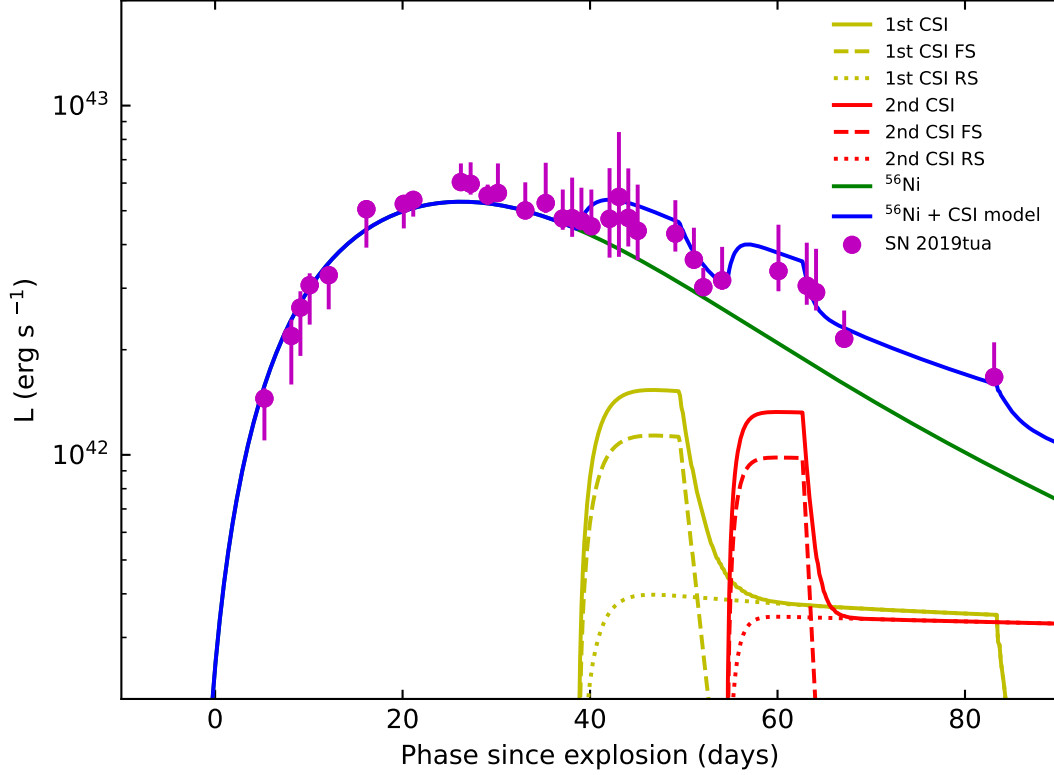


Figure 16. The bolometric LC of SN 2019tua reproduced by the double CSI plus the ^{56}Ni model. The total luminosity L_{bolo} is represented by the solid blue curve, and the contribution of ^{56}Ni is represented by the solid yellow line. The contributions of the two consecutive CSI events are shown as different colors of dashed and dotted curves, with green representing the contribution of the first CSI event and red representing the contribution of the second CSI event. The contribution of the forward shock $L_{\text{inp,FS},i}$ in the CSI event is represented by a dashed line, while the contribution of the reverse shock $L_{\text{inp,RS},i}$ is shown as a dotted line.

Table 6. Parament of the CSI Plus ^{56}Ni Model

M_{Ni}	$\kappa_{\gamma,\text{Ni}}$	Interaction	s	κ	$M_{\text{ej},i}$	$M_{\text{CSM},i}$	$R_{\text{CSM},\text{in},i}$	ϵ_i	$\rho_{\text{CSM},\text{in},i}$	x_0	t_{expl}	$t_{\text{CSI},i}$	χ^2/dof	AIC	BIC
(M_{\odot})	($\text{cm}^2 \text{g}^{-1}$)	i th		($\text{cm}^2 \text{g}^{-1}$)	(M_{\odot})	(M_{\odot})	(10^{14}cm)		($10^{-12} \text{g cm}^{-3}$)		(days)	(days)			
$0.41^{+0.01}_{-0.01}$	$0.01^{+0.00}_{-0.01}$	1	0	$0.17^{+0.01}_{-0.00}$	$2.03^{+0.05}_{-0.02}$	$0.38^{+0.06}_{-0.02}$	$7.10^{+2.18}_{-2.09}$	$0.32^{+0.03}_{-0.01}$	$29.26^{+3.27}_{-2.58}$	$0.18^{+0.01}_{-0.00}$	$-2.65^{+0.45}_{-0.67}$	$38.62^{+1.15}_{-1.44}$	0.85	43.69	151.85
		2	0		2.41	$0.63^{+0.15}_{-0.09}$	14.81	$0.24^{+0.06}_{-0.03}$	$49.30^{+4.99}_{-9.49}$			$54.55^{+2.29}_{-1.82}$			

NOTE— The uncertainties are 1σ .

(Chatzopoulos et al. 2012) assumed a stationary photosphere within the CSM, due to its lower expansion velocity compared to SN ejecta, allowing the bolometric LC to be expressed as:

$$L_{\text{CSI}}(t) = \frac{1}{t_0} e^{-\frac{t}{t_0}} \int_{t_{\text{expl}}}^{t+t_{\text{expl}}} e^{\frac{t'}{t_0}} \times [L_{\text{inp,FS}}(t') + L_{\text{inp,RS}}(t')] dt', \quad (4)$$

where $L_{\text{inp,FS}}(t')$ and $L_{\text{inp,RS}}(t')$ are the input luminosities from the forward shock (FS) and reverse shock (RS), $t_0 = \frac{\kappa M_{\text{CSM,th}}}{\beta c R_{\text{ph}}}$ is the diffusion timescale in the optically thick CSM (Chatzopoulos et al. 2012, 2013; Wang et al. 2017). $M_{\text{CSM,th}}$ and R_{ph} are the mass and the photospheric radius of the optically thick CSM, respectively.

The CSI model has eight parameters: the ejected mass M_{ej} (M_{\odot}), the mass of the collided CSM M_{CSM}

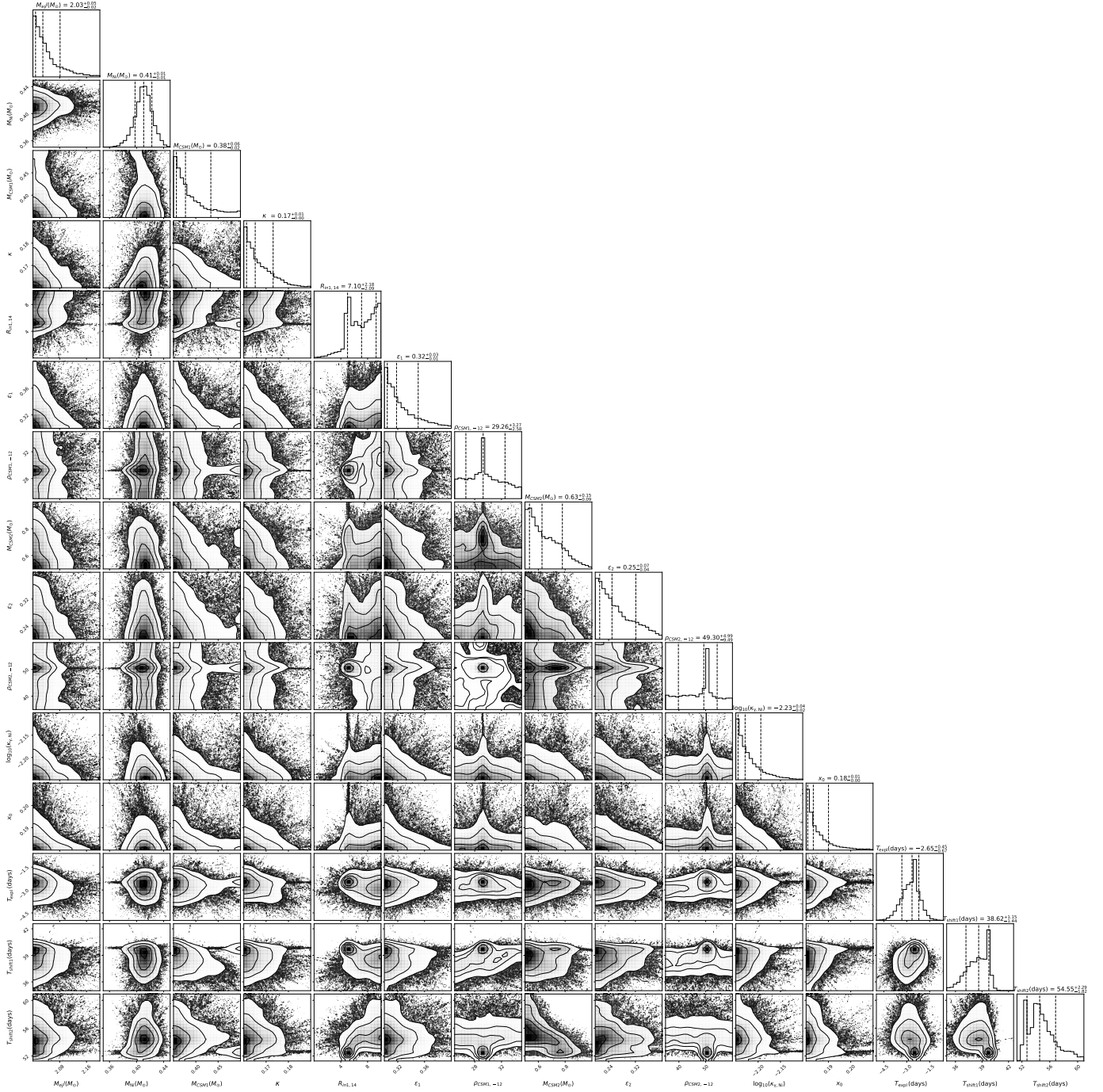


Figure 17. The corner plot for the CSI plus ^{56}Ni model. The uncertainties are computed as the 16th and 84th percentiles (1σ) of the posterior samples along each axis.

(M_{\odot}), the optical opacity κ ($\text{cm}^2 \text{g}^{-1}$), the density of the CSM ρ_{CSM} ($10^{-12} \text{g cm}^{-3}$), the initial radius of the collided CSM $R_{\text{CSM,in}}$ (10^{14}cm), the conversion efficiency of the shock energy into radiation ϵ , the dimensionless position parameter of break in the ejecta from the inner region to the outer region x_0 , the trigger moment of the interactions t_{expl} (days). The fitting results of the CSI model are illustrated in Figure 14 and summarized

in Table 5. And the corner plots of the CSI model are shown in Figure 15.

4.4. The CSI Plus ^{56}Ni Model

Although single-component models are effective in capturing general trends in luminosity evolution, they are unable to reproduce multiple bumps in the declining light curve. Here we present a multiple CSI model

to explain the complicated light curve of SN 2020tua. Such CSI model have been successfully applied to some SLSNe with bumpy features (Liu et al. 2018; Li et al. 2020; Lin et al. 2023). Considering the non-negligible contribution of the decay of $^{56}\text{Ni}/\text{Co}$, a comprehensive model should include both CSI and radioactive decay. The hybrid CSI plus ^{56}Ni model for output luminosity considers two distinct cases: a homogeneously expanding photosphere and a fixed photosphere. The expanding photosphere model is used for centrally located energy sources that heat the SN ejecta as it expands, whereas the fixed photosphere model is typically employed in CSI scenarios where the almost stationary CSM relative to the ejecta is heated. Thus the semi-analytic CSI plus ^{56}Ni model can be written as (Liu et al. 2018; Li et al. 2020; Lin et al. 2023)³:

$$L_{\text{bol}}(t) = \sum_i^N \frac{1}{t_{0,i}} e^{-\frac{t}{t_{0,i}}} \int_0^t e^{\frac{t'}{t_{0,i}}} \times [L_{\text{inp,FS},i}(t') + L_{\text{inp,RS},i}(t')] dt' + \frac{2}{\tau_m} e^{-\frac{t^2}{\tau_m^2}} \int_0^t e^{\frac{t'^2}{\tau_m^2}} \frac{t'}{\tau_m} L_{\text{inp,Ni}}(t') dt', \quad (5)$$

where the diffusion timescale can be written as $t_{0,i} = \sum_{j=i}^N \frac{\kappa_j M_{\text{CSM,th},j}}{\beta c R_{\text{ph}}}$. In this scenario, the main peak is mainly produced by the decay of ^{56}Ni , while the bumps in the declining light curve is powered by the CSI. It is reasonable to assume that there are at least two collisions between the SN ejecta and the CSM.

There are several free parameters that need to be carefully considered: the gamma-ray opacity of ^{56}Ni decay photons κ_γ ($\text{cm}^2 \text{g}^{-1}$), the optical opacity κ ($\text{cm}^2 \text{g}^{-1}$), the $M_{\text{ej},i}$ (M_\odot) is the initial ejecta mass of the i th interaction with $M_{\text{ej},2} = M_{\text{ej},1} + M_{\text{CSM},1}$, $M_{\text{CSM},i}$ is the mass of the i th collided CSM, $R_{\text{CSM,in},i}$ is the initial radius of the i th collided CSM (10^{14} cm) with $R_{\text{CSM,in},2} = R_{\text{CSM,in},1} + v_{\text{SN}}(t_{\text{CSI},2} - t_{\text{CSI},1})$, ϵ_i is the efficiency of the kinetic energy convert to radiation of the i th interaction, $\rho_{\text{CSM,in},i}$ ($10^{-12} \text{g cm}^{-3}$) is the density of the CSM at $R_{\text{CSM,in},i}$, the dimensionless position parameter of break in the ejecta from the inner region to the outer region x_0 , the epoch of the explosion t_{expl}

³ For hydrogen-rich SNe, such as type II-P SNe, which have a more abundant outer layer of hydrogen compared to other SNe, there is a need to consider a higher value for the optical opacity κ (Moriya et al. 2011; Wang et al. 2018; Chatzopoulos et al. 2012). That is because hydrogen-rich SNe originate from progenitor stars with massive hydrogen envelopes. The energy released from the recombination occurring in the extended hydrogen envelope of the progenitor manifests as a longer plateau feature in the light curve of hydrogen-rich SNe, rather than just small bumps.

(days), the time of the i th interaction between the ejecta and the i th CSM $t_{\text{CSI},i}$ (days).

The LC produced by the CSI plus ^{56}Ni model are show in Figure 16 and the best-fit parameters are listed in Table 6. And the corner plots of CSI plus ^{56}Ni model are shown in Figure 17.

5. DISCUSSION AND CONCLUSION

5.1. The Properties of SN 2019tua

Acrodding to the model that the CSI plus ^{56}Ni model, the best-fitting parameters are $M_{\text{Ni}} = 0.41_{-0.01}^{+0.01} M_\odot$ and $M_{\text{ej}} = 2.41 M_\odot$. The kinetic energy of SN 2019tua can be calculated, $\sim 0.5 \times 10^{51}$ erg. SN 2019tua has a lower kinetic energy compared to those of some SNe IIb: SN 2017gpn $\sim 3 \times 10^{51}$ erg (Balakina et al. 2021); SN 2020acat $\sim 1.2 \times 10^{51}$ erg (Medler et al. 2022); SN 2011fu $\sim 1.3 \times 10^{51}$ erg (Morales-Garoffolo et al. 2015); ASASSN-14dq $\sim 1.24 \times 10^{51}$ erg (Singh et al. 2018); SN 2020cxd $\sim 4.3 \times 10^{51}$ erg (Yang et al. 2021); SN 2003bg $\sim 5 \times 10^{51}$ erg (Hamuy et al. 2009). On the other hand, we can derive the mass-loss history of the event. Let $\Delta t'$ denote the time interval between the ejection and the collision of the ejecta with the CSM, and let $\Delta t = t_{\text{CSI}} - t_{\text{expl}}$ signify the interval between the SN explosion and the moment of shell collision. Thus, we have $v_{\text{SN}} \Delta t = v_{\text{shell}} (\Delta t' + \Delta t)$, yielding $\Delta t' = (v_{\text{SN}}/v_{\text{shell}} - 1) \Delta t$. According to literature, the velocity of the progenitor shell for a type II SN ranges from 20 to 100 km s^{-1} (Smith 2014). For SN 2019tua, with an observed velocity v_{SN} of approximately 5600 km s^{-1} , and Δt_{inner} around 41.3 days, the derived time scale for the mass loss from the inner shell spans approximately 6.2 to 31.6 years ($\sim 2271.5 - 11522.7$ days). For Δt_{outer} approximately 57.2 days, the time scale for the mass loss from the outer shell is estimated to be 8.6 to 43.7 years ($\sim 3146.0 - 15958.5$ days).

5.2. The Best Model

From a χ^2/dof standpoint, the ^{56}Ni model yields a satisfactory $\chi^2/\text{dof} = 0.37$. Magnetar models offer a superior fit to the data, evidenced by a χ^2/dof value of 0.98, although corroborative evidence for a magnetar-powered SN 2019tua is lacking (Vallely et al. 2018). Given the ongoing interactions between the SN ejecta and the CSM, especially near peak brightness, a single CSI model fits the data acceptably, attaining a χ^2/dof value of 0.35. However, this model fails to accurately capture the secondary peak in the LC following the initial brightness peak. Upon conducting AIC/BIC tests (with results detailed in accompanying tables), we find that the CSI plus ^{56}Ni model scores the highest, indicating its relative instability compared to other single models. Contrast-

ingly, the ^{56}Ni model most closely aligns with statistical criteria, displaying the lowest χ^2/dof and AIC/BIC values. In essence, no individual model can adequately account for the unique spectral features observed in SN 2019tua.

Additional spectral data offer further insights; narrow emission lines are discernible in the early spectra. And we have simply compared the redshift ($z = 0.010$) of the host galaxy with the narrow emission lines in the spectrum SN 2019tua in the TNS⁴, which are likely to originate from the host H II regions (Gutiérrez et al. 2017). Moreover, there is unclear visible spectral feature of separation between H-shell and He-shell in Figure 4, but there is obvious spectral feature of separation between H-shell and He-shell in Figure 5. The role of ^{56}Ni production during the SN explosion is non-negligible. The presence of bumps in the LC is highly likely associated with interactions with the CSM. Taking into account the above situation, we adopted the CSI plus ^{56}Ni model, which also yielded a good χ^2/dof value of 0.85. Although the χ^2/dof value may not fully elucidate these models due to uncertainties, the multi-component CSI plus ^{56}Ni model remains the most congruent with observed phenomena, and we also cannot rule out the possibility of the magnetar-powered model.

In this paper, we conducted comprehensive observations in the *BVRI* bands around the peak brightness of SN 2019tua and undertook extensive optical follow-up studies post-peak. Spectroscopically, the amalgamation of rising and near-peak spectra enabled a preliminary analysis of SN 2019tua. The combined photometric and essential spectroscopic data categorize SN 2019tua as a type IIb SN with robust observational evidence.

Data analysis reveals several key characteristics of the SN. Firstly, the spectrum of SN 2019tua displays a weak $\text{H}\alpha$ line and a narrow emission line, as well as a pronounced He absorption line, signifying the presence of CSM surrounding the progenitor. Given that the L_{peak} of SN 2019tua exceeds that of certain type Ib SNe, a correlation with type Ib SNe is thereby confirmed. These observations collectively indicate that the progenitor of SN 2019tua had a low-mass, mostly H-stripped envelope, leaving only a thin H envelope and an exposed He layer (Meza et al. 2020). While the spectral features broadly align with other type IIb SNe, its bolometric LC appears to be comparatively brighter, necessitating further investigation.

SN 2019tua has a well-constrained explosion date. Unlike typical type IIb SNe, its LC lacks an early-time de-

cline associated with a shock-cooling tail. SN 2019tua reached peak brightness approximately 25 days post-explosion, with a rate of brightness increase consistent with other type IIb SNe. Subsequently, a luminosity “bump” indicated interaction between the SN ejecta and CSM, suggestive of dense shells in the circumstellar environment. Various factors could contribute to such mass loss from the progenitor, and multiple shells resulting in a bumpy LC are conceivable.

After fitting the observed bolometric LC with three models, we conclude that SN 2019tua cannot be solely powered by the radioactive decay of ^{56}Ni . Additionally, while no bursts of gamma-rays or X-rays were detected at the same location, we cannot rule out the possibility of a magnetar model. A light curve primarily driven by radioactive decay of a moderate amount of ^{56}Ni , augmented by CSM interaction, better replicates the observed behavior of SN 2019tua. To account for the late LC bump, we employed a multiple-shell CSI model, with input parameters remaining within reasonable ranges.

In summary, the CSI model is substantiated by the presence of P–Cygni lines, suggesting that the progenitor of SN 2019tua with such features likely eject substantial amounts of material. This finding aligns with other observational results, such as luminosity fluctuations attributed to minor collisions. Despite SN 2019tua has a relatively brighter luminosity compared to other type IIb SNe, SN 2019tua can be explained through CSI and radioactive decay, negating the necessity for additional energy sources. The CSI plus ^{56}Ni model suggests that the progenitor of SN 2019tua had a pre-SN eruption. Multiple ejections before the explosion formed a multi-layered dense circumstellar shell around the SN. And the pre-SN eruption of SN 2019tua may produced by different mechanisms such as pulsational pair-instability supernova that undergo pulsations induced by pair production that may eject multiple interacting shells (Woosley et al. 2007), radiatively driven stellar winds that shed its envelope (Crowther 2007), waves propagating through the star’s envelope may produce dense CSM in the few years leading up to core collapse (Smith et al. 2014). In the context of binary companion, the scenarios surrounding mass loss become considerably more intricate (Sun et al. 2020).

The distinctive bumps and high luminosity observed in SN 2019tua stand out when compared to other SNe of the same classification. These features are likely a result of significant mass loss from SN 2019tua’s progenitor, which might have been more substantial than that experienced by progenitors of other type IIb SNe. This extensive mass loss likely led to the formation of multiple dense layers of CSM around SN 2019tua. The

⁴ <https://www.wis-tns.org/object/2019tua>

interaction between the ejecta and these denser layers of CSM, coupled with the ongoing energy contribution from the radioactive decay of ^{56}Ni , are key to explaining SN 2019tua's higher luminosity and the presence of bumps in its light curve following the main peak. This scenario, supported by our ^{56}Ni +CSM hybrid model, suggests that the unique interplay between enhanced mass loss, CSI, and nuclear decay significantly influences the observable characteristics of SN 2019tua, setting it apart from its type IIb counterparts. Additionally, SN 2018ivc also powered by CSM interaction with SN ejecta, SN 2018ivc exhibits early cooling emission is a result of the SN shock breaking out of the stellar envelope, followed by multiple smaller bumps after its main peak (Maeda et al. 2023). That suggests that the outer envelope mass mass of SN 2019tua is likely less than that of SN 2018ivc, resulting in SN 2019tua's in-

ability to produce a early cooling emission but rather generating bumps after its main peak.

6. ACKNOWLEDGEMENTS

We are thankful to the referee very much for useful comments and constructive suggestions. This study is supported by the National Natural Science Foundation of China (grant Nos. 12373042, U1938201, 12133003, 12303050, 11973055 and 12173009), the Programme of Bagui Scholars Programme (WXG) and the Guangxi Science Foundation (grant Nos. 2020GXNSFDA238018). We acknowledge the support of the staff of the Xinglong 2.16m telescope. This work was partially supported by the Open Project Program of the Key Laboratory of Optical Astronomy, National Astronomical Observatories, Chinese Academy of Sciences.

REFERENCES

- Afsariardchi, N., Drout, M. R., Khatami, D. K., Matzner, C. D., Moon, D.-S., Ni, Y. Q. 2021, *ApJ*, 918, 89, doi:10.3847/1538-4357/ac0aeb
- Andrews, J. E., Sand, D. J., Valenti, S., Smith, N., Dastidar, R., Sahu, D. K., et al. 2019, *ApJ*, 885, 43, doi:10.3847/1538-4357/ab43e3
- Arcavi, I., Gal-Yam, A., Yaron, O., Sternberg, A., Rabinak, I., Waxman, E., Kasliwal, et al. 2011, *ApJ*, 742, L18, doi:10.1088/2041-8205/742/2/L18
- Armstrong, P., Tucker, B. E., Rest, A., Ridden-Harper, R., Zenati, Y., Piro, A. L., et al. 2021, *MNRAS*, 507, 3125-3138, doi:10.1093/mnras/stab2138
- Arnett, W. D. 1980, *ApJ*, 237, 541-549, doi:10.1086/157898
- Arnett, W. D. 1982, *ApJ*, 253, 785-797, doi:10.1086/159681
- Balakina, E. A., Pruzhinskaya, M. V., Moskvitin, A. S., Blinnikov, S. I., et al. 2021, *MNRAS*, 501, 5797-5810, doi:10.1093/mnras/staa3383
- Bersten, M. C., Benvenuto, O. G., Nomoto, K., Ergon, M., Folatelli, G., Sollerman, J., Benetti, S., et al. 2012, *ApJ*, 757, 31, doi:10.1088/0004-637X/757/1/31
- Bose, S., Sutaria, F., Kumar, B., Duggal, C., Misra, K., et al. 2015, *ApJ*, 806(2), 160, doi:10.1088/0004-637X/806/2/160
- Bose, Subhash and Dong, Subo and Kochanek, C. S. and Stritzinger, M. D. and Ashall, et al. 2021, *MNRAS*, 503, 3472-3491, doi:10.1093/mnras/stab629
- Breedt, E. 2019, in *Southern Horizons in Time-Domain Astronomy*, ed. R. Elizabeth Griffin, IAU Symposium, 339, 12-15, doi:10.1017/S1743921318002090
- Brown, T. M., Baliber, N., Bianco, F. B., Bowman, M., Burleson, B., Conway, P., Crellin, M., et al. 2013, *PASP*, 125, 1031, doi:10.1086/673168
- Burke, J., Hiramatsu, D., Howell, D. A., McCully, C., Pellegrino, C., 2019, *Transient Name Server Classification Report*, 2019-2244, 1
- Chambers, K. C., Magnier, E. A., Metcalfe, N., Flewelling, H. A., Huber, M. E., et al. 2016, arXiv, arXiv:1612.05560, doi:10.48550/arXiv.1612.05560
- Chatzopoulos, E., Wheeler, J. Craig, Vinko, J. 2012, *ApJ*, 746, 121, doi:10.1088/0004-637X/746/2/121
- Chatzopoulos, E., Wheeler, J. Craig, Vinko, J., Horvath, Z. L., Nagy, A. 2013, *ApJ*, 773, 76, doi:10.1088/0004-637X/773/1/76
- Chevalier, Roger A., Fransson, Claes 1994, *ApJ*, 420, 268, doi:10.1086/173557
- Colgate, Stirling A., McKee, Chester 1969, *ApJ*, 157, 623, doi:10.1086/150102
- Colgate, S. A., Petschek, A. G., Kriese, J. T. 1980, *ApJL*, 237, L81-L85, doi:10.1086/183239
- Crockett, R. M., Eldridge, J. J., Smartt, S. J., Pastorello, A., Gal-Yam, A., Fox, D. B., Leonard, D. C., et al. 2008, *MNRAS*, 391, L5-L9, doi:10.1111/j.1745-3933.2008.00540.x
- Crowther, P. A. 2007, *A&A*, 45, 1, 177-219, doi:10.1146/annurev.astro.45.051806.110615
- Davis, S., Pessi, P. J., Fraser, M., Ertini, K., Martinez, L., Hoeflich, P., et al. *ApJ*, 909(2), 145, doi:10.3847/1538-4357/abdd36

- Eldridge, John J., Fraser, Morgan, Smartt, Stephen J., Maund, Justyn R., Crockett, R. Mark 2013, MNRAS, 436, 774-795, doi:10.1093/mnras/stt1612
- Ergon, M., Sollerman, J., Fraser, M., Pastorello, A., Taubenberger, S., Elias-Rosa, N., Bersten, M., et al. 2014, A&A, 562, A17, doi:10.1051/0004-6361/201321850
- Ergon, M., Lundqvist, P., Fransson, C., Kuncarayakti, H., Das, K. K., De, K., et al. 2024, A&A, 683, A241, doi:10.1051/0004-6361/202346718
- Fan, Zhou, Wang, Huijuan, Jiang, Xiaojun, Wu, Hong, Li, Hongbin, Huang, Yang, Xu, Dawei, et al. 2016, PASP, 128, 115005, doi:10.1088/1538-3873/128/969/115005
- Filippenko, Alexei V. 1997, A&A, 35, 309, doi:10.1146/annurev.astro.35.1.309
- Folatelli, Gastón, Bersten, Melina C., Benvenuto, Omar G., et al. 2014, ApJL, 793, L22, doi:10.1088/2041-8205/793/2/L22
- Folatelli, Gastón and Bersten, Melina C. and Kuncarayakti, Hanindyo and Olivares Estay, et al. 2014, ApJ, 792, 1, 7, doi:10.1088/0004-637X/792/1/7
- Foreman-Mackey, Daniel, Hogg, David W., Lang, Dustin, & Goodman, Jonathan 2013, PASP, 125, 306, doi:10.1086/670067
- Fox, Ori D., Silverman, Jeffrey M., Filippenko, Alexei V., Mauerhan, Jon, Becker, Juliette, Borish, H. Jacob, et al. 2015, MNRAS, 447, 772-785, doi:10.1093/mnras/stu2435
- Fremling, C., Ko, H., Dugas, A., Ergon, M., Sollerman, J., Bagdasaryan, A., et al. 2019, ApJL, 878, L5, doi:10.3847/2041-8213/ab218f
- Gal-Yam, Avishay. 2017, in Handbook of Supernovae, eds. Alsabti, Athem W. & Murdin, Paul, 195, doi: 10.1007/978-3-319-21846-5_35
- Gangopadhyay, Anjasha and Misra, Kuntal and Pastorello, A. and Sahu, et al. 2018, MNRAS, 476, 3, doi: 10.1093/mnras/sty478
- Gutiérrez, C. P., Anderson, J. P., Hamuy, M., González-Gaitán, S., Folatelli, G., Morrell, N. I., Stritzinger, M. D., et al. 2014, ApJL, 786, L15, doi:10.1088/2041-8205/786/2/L15
- Gutiérrez, C. P., Anderson, J. P., Hamuy, M., Morrell, N., et al. 2017, ApJ, 850(1), 89, doi:10.3847/1538-4357/aa8f52
- Hamuy, M., Deng, J., Mazzali, P. A., Morrell, N. I., Phillips, M. M., Roth, M., Gonzalez, S., et al. 2009, ApJ, 703, 1612-1623, doi:10.1088/0004-637X/703/2/1612
- Heger, A., Fryer, C. L., Woosley, S. E., Langer, N., Hartmann, D. H. 2003, ApJ, 591, 288-300, doi:10.1086/375341
- Hosseinzadeh, G., Sand, D. J., Lundqvist, P., Andrews, J. E., Bostroem, K. A., Dong, Y., Janzen, D., et al. 2022, ApJL, 933, L45, doi:10.3847/2041-8213/ac7cef
- Huang, F., Wang, X., Zampieri, L., Pumo, M. L., Arcavi, I., Brown, P. J., et al. 2016, ApJ, 832(2), 139, doi:10.3847/0004-637X/832/2/139
- Kasen, Daniel & Bildsten, Lars. 2010, ApJ, 717, 245-249, doi:10.1088/0004-637X/717/1/245
- Kilpatrick, Charles D., Coulter, David A., Foley, Ryan J., Piro, Anthony L., Rest, Armin, Rojas-Bravo, César, Siebert, Matthew R. 2022, ApJ, 936, 111, doi:10.3847/1538-4357/ac8a4c
- Li, Long, Dai, Zi-Gao, Wang, Shan-Qin, Zhong, Shu-Qing. 2020, ApJ, 900, 121, doi:10.3847/1538-4357/aba95b
- Li, Long, Wang, Shan-Qin, Liu, Liang-Duan, Wang, Xiang-Gao, Liang, En-Wei, Dai, Zi-Gao. 2020, ApJ, 891, 98, doi:10.3847/1538-4357/ab718d
- Lin, Weili, Wang, Xiaofeng, Yan, Lin, Gal-Yam, Avishay, Mo, Jun, Brink, Thomas G., Filippenko, Alexei V., et al. 2023, Nature Astronomy, 7, 779-789, doi:10.1038/s41550-023-01957-3
- Liu, Liang-Duan, Wang, Ling-Jun, Wang, Shan-Qin, Dai, Zi-Gao. 2018, ApJ, 856, 59, doi:10.3847/1538-4357/aab157
- Maeda, K., Hattori, T., Milisavljevic, D., Folatelli, G., Drout, M. R., Kuncarayakti, H., Margutti, R., et al. 2015, ApJ, 807, 35, doi:10.1088/0004-637X/807/1/35
- Maeda, K., Chandra, P., Moriya, T. J., Reguitti, A., Ryder, S., et al. 2023, ApJ, 942(1), 17, doi:10.3847/1538-4357/aca1b7
- Margutti, R., Milisavljevic, D., Soderberg, A. M., Guidorzi, C., Morsony, B. J., Sanders, N., Chakraborti, S., et al. 2014, ApJ, 797, 107, doi:10.1088/0004-637X/797/2/107
- Martin, J. C., Hamsch, F. -J., Margutti, R., Tan, T. G., Curtis, I., Soderberg, A. 2015, AJ, 149, 9, doi:10.1088/0004-6256/149/1/9
- Maund, Justyn R. & Smartt, Stephen J. 2009, Science, 324, 486, doi:10.1126/science.1170198
- Maund, Justyn R., Smartt, Stephen J., Kudritzki, Rolf P., Podsiadlowski, Philipp, & Gilmore, Gerard F. 2004, Nature, 427, 129-131, doi:10.1038/nature02161
- Maund, J. R., Fraser, M., Ergon, M., Pastorello, A., Smartt, S. J., Sollerman, J., Benetti, S., et al. 2011, ApJL, 739, L37, doi:10.1088/2041-8205/739/2/L37
- Medler, K., Mazzali, P. A., Teffs, J., Ashall, C., Anderson, J. P., Arcavi, I., Benetti, S., et al. 2022, MNRAS, 513, 5540-5558, doi:10.1093/mnras/stac1192
- Medler, K., Mazzali, P. A., Teffs, J., Prentice, S. J., Ashall, C., et al. 2021, MNRAS, 1832-1849, doi:10.1093/mnras/stab1761

- Meza, N., Anderson, J. P. 2020, *A&A*, 641, A177, doi:10.1051/0004-6361/201937113
- Mnicholl. 2018, *superbol v1.0*, Zenodo, doi:10.5281/zenodo.2155821.
- Monet, D. G., Levine, S. E., Canzian, B., Ables, H. D., Bird, A. R., Dahn, C. C., et al. 2003, *AJ*, 125, 984, doi:10.1086/345888.
- Morales-Garoffolo, A., Elias-Rosa, N., Benetti, S., Taubenberger, S., Cappellaro, E., Pastorello, A., et al. 2014, *MNRAS*, 445, 1647, doi:10.1093/mnras/stu1837
- Morales-Garoffolo, A., Elias-Rosa, N., Bersten, M., Jerkstrand, A., Taubenberger, S., Benetti, S., et al. 2015, *MNRAS*, 454, 95, doi:10.1093/mnras/stv1972
- Moriya, Takashi, Tominaga, Nozomu, Blinnikov, Sergei I., Baklanov, Petr V., Sorokina, Elena I. 2011, *MNRAS*, 415, 199, doi:10.1111/j.1365-2966.2011.18689.x
- Nayana, A. J., Chandra, Poonam, Krishna, Anoop, Anupama, G. C. 2022, *ApJ*, 934, 186, doi:10.3847/1538-4357/ac7c1e
- Nicholl, M., Berger, E., Margutti, R., Blanchard, P. K., Milisavljevic, D., et al. 2017, *ApJL*, 835, L8, doi:10.3847/2041-8213/aa56c5
- Nomoto, K. I., Iwamoto, K., Suzuki, T. 1995, *PhR*, 256, 173-191, doi:10.1016/0370-1573(94)00107-E
- Nyholm, A., Sollerman, J., Taddia, F., Fremling, C., Moriya, T. J., et al. 2017, *A&A*, 605, A6, doi:10.1051/0004-6361/201629906
- Pastorello, A., Kasliwal, M. M., Crockett, R. M., Valenti, S., Arbour, R., et al. 2008, *MNRAS*, 389, 955-966, doi:10.1111/j.1365-2966.2008.13618.x
- Pastorello, A., Quimby, R. M., Smartt, S. J., Mattila, S., Navasardyan, H., et al. 2008, *MNRAS*, 389, 131-140, doi:10.1111/j.1365-2966.2008.13603.x
- Pessi, P. J., Folatelli, G., Anderson, J. P., Bersten, M., Burns, C., et al. 2019, *MNRAS*, 488(3), 4239-4257, doi:10.1093/mnras/stz1855
- Phillips, M. M., Simon, Joshua D., Morrell, Nidia, Burns, Christopher R., Cox, Nick L. J., et al. 2013, *ApJ*, 779, 38, doi:10.1088/0004-637X/779/1/38
- Podsiadlowski, Ph., Hsu, J. J. L., Joss, P. C., Ross, R. R. 1993, *Nature*, 364, 509, doi:10.1038/364509a0
- Podsiadlowski, Ph., Joss, P. C., Hsu, J. J. L. 1992, *ApJ*, 391, 246, doi:10.1086/171341
- Poznanski, Dovi, Ganeshalingam, Mohan, Silverman, Jeffrey M., Filippenko, Alexei V. 2011, *MNRAS*, 415, L81-L84, doi:10.1111/j.1745-3933.2011.01084.x
- Richmond, Michael W., Treffers, Richard R., Filippenko, Alexei V., Paik, Young, Leibundgut, Bruno et al. 1994, *AJ*, 107, 1022, doi:10.1086/116915
- Roy, R., Sollerman, J., Silverman, J. M., Pastorello, A., Fransson, C., Drake, A., Taddia, F., et al. 2016, *A&A*, 596, A67, doi:10.1051/0004-6361/201527947
- Ryder, S. D., Van Dyk, S. D., Fox, O. D., Zapartas, E., de Mink, S. E., Smith, N., Brunsden, E., et al. 2018, *ApJ*, 856, 83, doi:10.3847/1538-4357/aaaf1e
- Sahu, D. K., Anupama, G. C., Chakradhari, N. K. 2013, *MNRAS*, 433, 2-22, doi:10.1093/mnras/stt647
- Schlafly, E. F., Finkbeiner, D. P. 2011, *ApJ*, 737, 103, doi:10.1088/0004-637X/737/2/103
- Singh, A., Srivastav, S., Kumar, B., Anupama, G. C., Sahu, D. K. 2018, *MNRAS*, 480, 2475-2500, doi:10.1093/mnras/sty1957
- Smith, N., Li, W., Miller, A. A., Silverman, J. M., Filippenko, A. V. et al. 2011, *ApJ*, 732, 2, 63, doi:10.1088/0004-637X/732/2/63
- Smith, N., Arnett, W. D. 2014, *ApJ*, 785, 2, 82, doi:10.1088/0004-637X/785/2/82
- Smith, N. 2014, *ARA&A*, 52, 487, doi:10.1146/annurev-astro-081913-040025
- Soderberg, A. M., Margutti, R., Zauderer, B. A., Krauss, M., Katz, B. et al. 2012, *ApJ*, 752, 2, 78, doi:10.1088/0004-637X/752/2/78
- Smith, K. W., Smartt, S. J., Young, D. R., Tonry, J. L., Denneau, L. et al. 2021, *PASP*, 133, 1020, 029201, doi:10.1088/1538-3873/abd9da
- Srivastav, S., Smith, K. W., McBrien, O., Smartt, S. J., Gillanders, J., Chen, T. W., Denneau, L., Flewelling, H., Heinze, A., Tonry, J. et al. 2019, *Transient Name Server AstroNote*, 119, 1
- Stritzinger, M., Taddia, F., Fransson, C., Fox, O. D., Morrell, N. et al. 2012, *ApJ*, 756, 2, 173, doi:10.1088/0004-637X/756/2/173
- Sun, N.-C., Maund, J. R., Hirai, R., Crowther, P. A., Podsiadlowski, P. 2020, *MNRAS*, 491, 4, 6000-6019, doi:10.1093/mnras/stz3431
- Taddia, F. and Sollerman, J. and Leloudas, G. and Stritzinger, M. D. and Valenti et al. 2012, *A&A*, 574, A60, doi:10.1051/0004-6361/201423915
- Takáts, K., Pignata, G., Pumo, M. L., Paillas, E., Zampieri, L., et al. 2015, *MNRAS*, 450(3), 3137-3154, doi:10.1093/mnras/stv857
- Tartaglia, L., Sand, D. J., Groh, J. H., Valenti, S., Wyatt, S. D., et al. 2021, *ApJ*, 907(1), 52, doi:10.3847/1538-4357/abca8a
- Teja, R. S., Singh, A., Sahu, D. K., Anupama, G. C., et al. 2022, *ApJ*, 930(1), 34, doi:10.3847/1538-4357/ac610b

- Tody, D. 1986, in *Society of Photo-Optical Instrumentation Engineers (SPIE) Conference Series*, vol. 627, *Instrumentation in astronomy VI*, ed. D. L. Crawford, 733, doi:10.1117/12.968154
- Teffs, J. and Mazzali, P. A. and Medler, K. and Hachinger, S., 2022, *MNRAS*, 517, 4, 5678-5686, doi:10.1093/mnras/stac3077
- Tonry, J., Denneau, L., Heinze, A., Weiland, H., Flewelling, H. et al. 2019, *Transient Name Server Discovery Report*, 2019-2232, 1
- Tonry, J. L., Denneau, L., Heinze, A. N., Stalder, B., Smith, K. W., et al. 2018, *PASP*, 130, 988, 064505, doi:10.1088/1538-3873/aabadf
- Terreran, G., Jerkstrand, A., Benetti, S., Smartt, S. J., Ochner, P., et al. 2016, *MNRAS*, 462(1), 137-157, doi:10.1093/mnras/stw1591
- Vallely, P. J., Prieto, J. L., Stanek, K. Z., Kochanek, C. S., Sukhbold, T., et al. 2018, *MNRAS*, 475, 2, 2344-2354, doi:10.1093/mnras/stx3303
- Van Dyk, S. D., Zheng, W., Fox, O. D., Cenko, S. B., Clubb, K. I. et al. 2014, *AJ*, 147, 2, 37, doi:10.1088/0004-6256/147/2/37
- Virtanen, P., Gommers, R., Oliphant, T. E., Haberland, M., Reddy, T., et al. 2020, *Nature Methods*, 17, 261-272, doi:10.1038/s41592-019-0686-2
- Wang, L. J., Cano, Z., Wang, S. Q., Zheng, W. K., Liu, L. D., et al. 2017, *ApJ*, 851, 54, doi:10.3847/1538-4357/aa9a38
- Wang, L. J., Wang, X. F., Wang, S. Q., Dai, Z. G., Liu, L. D., Song, L. M., Rui, L. M., Cano, Z., Li, B. 2018, *ApJ*, 865, 2, 95, doi:10.3847/1538-4357/aadba4
- Wang, S. Q., Wang, L. J., Dai, Z. G., Wu, X. F. 2015, *ApJ*, 807, 147, doi:10.1088/0004-637X/807/2/147
- Woosley, S. E., Blinnikov, S., Heger, Alexander 2007, *Nature*, 450, 390, doi:10.1038/nature06333
- Woosley, S. E., Eastman, Ronald G., Weaver, Thomas A., Pinto, Philip A. 1994, *ApJ*, 429, 300, doi:10.1086/174319
- Xu, Y., Xin, L. P., Wang, J., Han, X. H., Qiu, Y. L., Huang, M. H., Wei, J. Y. 2020, *PASP*, 132, 1011, 054502, doi:10.1088/1538-3873/ab7a73
- Yadav, N., Ray, A., Chakraborti, S., Stockdale, C., Chandra, P., et al. 2014, *ApJ*, 782(1), 30, doi:10.1088/0004-637X/782/1/30
- Yan, L., Quimby, R., Gal-Yam, A., Brown, P., Blagorodnova, N. et al. 2017, *ApJ*, 840, 1, 57, doi:10.3847/1538-4357/aa6b02
- Yang, S., Sollerman, J., Strotjohann, N. L., Schulze, S., Lunnan, R. et al. 2021, *A&A*, 655, A90, doi:10.1051/0004-6361/202141244
- Zacharias, N., Monet, D. G., Levine, S. E., Urban, S. E., Gaume, R., Wycoff, G. L. 2004, *American Astronomical Society Meeting Abstracts*, 205, 48.15
- Zhang, J., Wang, X., József, V., Zhai, Q., Zhang, T., Filippenko, A. V., et al. 2020, *MNRAS*, 498(1), 84-100, doi:10.1093/mnras/staa2273